Mon. Not. R. Astron. Soc. **000**, 000–000 (0000) Printed 12 October 2011 (MN LATEX style file v2.2)

Precision simulation of ground-based lensing data using observations from space

Rachel Mandelbaum[1⋆], Christopher M. Hirata[2], Alexie Leauthaud[3], Richard J. Massey[4], Jason Rhodes[5]
[1] *Department of Astrophysical Sciences, Princeton University, Peyton Hall, Princeton, NJ 08544, USA*
[2] *Department of Astronomy, Caltech M/C 350-17, Pasadena, CA 91125, USA*
[3] *Lawrence Berkeley National Laboratory, Berkeley, CA 94720, USA*
[4] *Institute for Astronomy, Royal Observatory, Blackford Hill, Edinburgh EH9 3HJ, UK*
[5] *Jet Propulsion Laboratory, California Institute of Technology, Pasadena, CA 91109*

arXiv:1107.4629v2 [astro-ph.CO] 11 Oct 2011

12 October 2011

ABSTRACT

Current and upcoming wide-field, ground-based, broad-band imaging surveys promise to address a wide range of outstanding problems in galaxy formation and cosmology. Several such uses of ground-based data, especially weak gravitational lensing, require highly precise measurements of galaxy image statistics with careful correction for the effects of the point-spread function (PSF). In this paper, we introduce the SHERA (SHEar Reconvolution Analysis) software to simulate ground-based imaging data with realistic galaxy morphologies and observing conditions, starting from space-based data (from COSMOS, the Cosmological Evolution Survey) and accounting for the effects of the space-based PSF. This code simulates ground-based data, optionally with a weak lensing shear applied, in a model-independent way using a general Fourier space formalism. The utility of this pipeline is that it allows for a precise, realistic assessment of systematic errors due to the method of data processing, for example in extracting weak lensing galaxy shape measurements or galaxy radial profiles, given user-supplied observational conditions and real galaxy morphologies. Moreover, the simulations allow for the empirical test of error estimates and determination of parameter degeneracies, via generation of many noise maps. The public release of this software, along with a large sample of cleaned COSMOS galaxy images (corrected for charge transfer inefficiency), should enable upcoming ground-based imaging surveys to achieve their potential in the areas of precision weak lensing analysis, galaxy profile measurement, and other applications involving detailed image analysis.

Key words: methods: data analysis – techniques: image processing – gravitational lensing: weak – galaxies: structure

1 INTRODUCTION

A tremendous variety of measurements are carried out on astronomical images from ground-based telescopes. A generic problem that often arises is the question of how the intrinsically limited resolution of ground-based images (both due to convolution with the atmospheric point-spread function, or PSF, and due to the finite pixel size) affects our ability to measure quantities such as the radial profiles of galaxies $I(r)$, or statistics of the profile such as its slope, half-light radius, and ellipticity. Moreover the error distributions of these parameters, which are often estimated via a highly non-linear fitting procedure, are also unclear in many circumstances.

One application that particularly suffers from such uncertainties is the field of weak gravitational lensing (for a review, see Bartelmann & Schneider 2001, Refregier 2003a, Hoekstra & Jain 2008, or Massey et al. 2010a). In the past decade, weak lensing has been used extensively for measurements that can constrain cosmology and galaxy formation. Cosmic shear measurements have constrained cosmological parameters (e.g., most recently, Fu et al. 2008; Schrabback et al. 2010); cluster lensing analyses (e.g., Hoekstra 2007; Okabe et al. 2010) have been used to understand the most massive structures in the universe, the abundance of which can constrain cosmology through the mass function (e.g., Rines et al. 2007;

⋆ rmandelb@astro.princeton.edu

© 0000 RAS

Mantz et al. 2008; Vikhlinin et al. 2009; Rozo et al. 2010); and galaxy-galaxy lensing measurements have probed the connection between galaxies, their dark matter halos, and their larger scale environments (Schulz et al. 2010; Leauthaud et al. 2011), as well as constraining the theory of gravity on cosmological scales when combined with other observational methods (Reyes et al. 2010). The next decade promises a larger volume of weak lensing data that can be used for more precise constraints on cosmology and galaxy formation, from surveys such as Hyper Suprime-Cam (HSC, Miyazaki et al. 2006), Dark Energy Survey (DES[1], Dark Energy Survey Collaboration 2005), the KIlo-Degree Survey (KIDS[2]), the Panoramic Survey Telescope and Rapid Response System (Pan-STARRS[3], Kaiser et al. 2010); and even more ambitious programmes are planned such as the Large Synoptic Survey Telescope (LSST[4], LSST Science Collaborations 2009), Euclid[5], and the Wide-Field Infrared Survey Telescope (WFIRST[6]).

Weak lensing measurements depend on precise measurements of the shapes of galaxies, in an attempt to infer the apparent shape distortions in distant 'source' galaxies due to the mass in nearby 'lenses' (galaxies, clusters, or other mass distributions). Weak lensing is a statistical measurement, with averages over large numbers of sources in order to detect the ~ 0.1–1 per cent level distortions within the noise of the intrinsic galaxy ellipticities, which are typically a factor of ~ 100 larger. Unfortunately, coherent systematic distortions of galaxy shapes due to the PSF caused by the atmosphere (for a ground-based telescope), telescope optics, and detector are significantly larger than typical weak lensing distortions, which means that accurate PSF-correction is critical for current lensing studies, and all the more so for future lensing surveys that aim for < 1 per cent statistical errors.

The weak lensing community has had several challenges, using blind simulations, to identify the most promising methods of PSF correction. The first of these, the Shear TEsting Programme-1 (STEP1; Heymans et al. 2006), included mock galaxies with idealized radial profiles and several PSFs meant to mimic specific observational issues (e.g., astigmatism). The second, STEP2 (Massey et al. 2007a), used shapelets (Refregier 2003b; Refregier & Bacon 2003) decompositions of COSMOS galaxies (including the COSMOS PSF, for which no correction was imposed) as inputs, and then convolved them with a variety of ground-based PSFs from Subaru Suprime-Cam (Miyazaki et al. 2002). Finally, the GRavitational lEnsing Accuracy Testing-08 (GREAT08; Bridle et al. 2009, 2010) and GREAT10 (Kitching et al. 2010) challenges reverted to composite model galaxies (based on Sérsic profiles; Sérsic 1968) with very specific sets of parameters, and tested the recovery of the shear as a function of image S/N, PSF size, and galaxy profile type. All of these challenges were useful to the lensing community in different ways, and in some cases led to changes in attitudes towards (or a greater understanding of) common methods of PSF correction. However, their ability to identify, in a broad sense, the most promising methods of PSF correction does not mean that they can be used to constrain, to high precision, the shear calibration in all lensing observations using those PSF-correction methods[7]. There are numerous reasons why this is the case, such as galaxy models and observing conditions (PSF and depth) that are not representative of a particular survey. STEP2 (Massey et al. 2007a) showed that the shear systematics for nearly every method of PSF correction depend on the observing conditions (the galaxy S/N and resolution compared to the PSF); GREAT08 (Bridle et al. 2010) showed a dependence on galaxy type as well.

More recent work has shown that the dependence of shear calibration factors on the galaxy population is generic. In particular, Massey et al. (2007b) and Zhang & Komatsu (2011) showed that there is *no* stable shape measurement algorithm on finite-resolution data whose shear calibration factor is independent of the galaxy population[8]. Instead, Bernstein (2010) and Zhang & Komatsu (2011) argue that the same lensing survey that measures shear could also determine the range of galaxy models presented to us by the real Universe. While we will explore this point in more detail in Sec. 3, we conclude that to precisely constrain the shear calibration or understand observational selection biases in any given survey, the simulations must have realistic galaxy models as well as observing conditions.

When constraining systematic errors in ground-based lensing data, we may wish to use space-based data as the basis of our simulations, due to its much higher resolution. Indeed, one might ask why simulations are needed at all: can we simply rely on comparison with PSF-corrected shapes on space-based images? This approach was taken by Kasliwal et al. (2008), who compared shape measurements using a KSB-based method (Kaiser et al. 1995; Hamana et al. 2003) on Subaru data against shape measurements using the RRG method (Rhodes et al. 2000) on COSMOS data. However, there are some limitations to this approach. First, if one wishes to avoid complications due to a non-negligible PSF and therefore the need for substantial PSF correction in the space-based data, the comparison must be restricted to a subset of larger galaxies, as in Kasliwal et al. (2008). More importantly, such a direct comparison of the derived shapes or shears is not possible at all

[1] https://www.darkenergysurvey.org/
[2] http://www.astro-wise.org/projects/KIDS/
[3] http://pan-starrs.ifa.hawaii.edu/public/
[4] http://www.lsst.org/lsst
[5] http://sci.esa.int/science-e/www/area/index.cfm?fareaid=102
[6] http://wfirst.gsfc.nasa.gov/

[7] The validity of this statement depends on the data for which the shear calibration is desired. For example, the STEP2 simulations are likely to give a more realistic estimate of the calibration for the Subaru Suprime-Cam data that it was designed to mimic than for data from some other telescope (assuming that image combination and other steps in a realistic data analysis, which were not simulated, do not introduce additional biases).

[8] The argument hinges on the existence of a finite number of well-measured moments M_{ij} of the galaxy, and the fact that the dependence of the M_{ij} on shear ($\partial M_{ij}/\partial\gamma_k$) is determined in part by higher, unmeasured moments. A related issue occurs in Fourier space: when attempting to define a roundness test for a sheared galaxy, Bernstein (2010, last paragraph of section 4.2) finds that the finite extent of the modulation transfer function (MTF) prevents such a test from being shear-covariant, and argues that the issue is generic.

for some shape measurement methods if the ellipticities are defined in incompatible ways, as will be explained at greater detail later in this paper (Sec. 4.3). We thus conclude that, rather than carrying out a catalogue-level comparison, we should use the space-based data to make realistic simulations of ground-based lensing data, to which a shear can be added and shear recovery can be tested.

In this paper, we therefore have three goals. First, we outline a method for simulating ground-based lensing data using higher-resolution data from space, including a careful treatment of the original space-based PSF and pixel sampling, and conversion to the new ground-based PSF and pixel sampling, inspired by Kaiser (2000). This method will allow the galaxies to be sheared, so that we can test the recovery of gravitational shear, including the many types of selection biases and PSF effects such as those described in Hirata et al. (2004) and Mandelbaum et al. (2005). This method is a model-free generalization of that used in Dobke et al. (2010), which relies on shapelets decompositions (Gauss-Laguerre basis functions) and therefore depends on the galaxy profiles and PSFs being well-described by sums of these functions to some finite order. Given that this assumption is not necessarily true for realistic galaxies and PSFs (e.g., Melchior et al. 2010), the advantage of a model-independent image simulation method is clear. Second, we describe a publicly-released implementation of this method in IDL. We emphasize that, while this paper focuses on weak gravitational lensing, this simulation pipeline is equally applicable to many other science analyses that are commonly done using ground-based data, for example modeling of galaxy radial profiles. Finally, we demonstrate the method by simulating Sloan Digital Sky Survey (SDSS) lensing data, and show how these simulations can be used to estimate shear systematics in SDSS to high precision. This will be of practical use for interpreting past lensing measurements that used the SDSS shape catalogue we simulate, and eventually for reducing the systematic error budgets in future papers using that catalogue.

We begin in Section 2 by describing weak gravitational lensing and its effects on galaxy shapes. Section 3 describes the process of removing the effects of the PSF from measured galaxy shapes, so that lensing can be measured. The space-based data that are used as the basis of these simulations, and the ground-based data that we simulate in this paper, are described in Section 4. In Section 5, we describe the methodology that will be used to create accurate simulations of ground-based data. We describe steps that we took to prepare the space-based data for this purpose in Section 6, and our specific implementation of the simulation method in Section 7. Technical tests of this implementation are presented in Section 8, and an example of how the SHERA outputs can be used to test galaxy shape measurements is in Section 9. We discuss these results in Section 10.

2 WEAK LENSING BASICS

Gravitational lensing is the deflection of light from distant objects ('sources') by all mass, including dark matter, along the line of sight ('lenses'). Typically, it results in a weak but coherent distortion in the shapes of distant galaxies (weak lensing). This distortion can be quantified by considering the true source position $\boldsymbol{\beta}$ and the observed position $\boldsymbol{\theta}$ with respect to the lens; instead of the intrinsic surface brightness profile $I(\boldsymbol{\beta})$, we observe a perturbed profile $I(\boldsymbol{\theta}(\boldsymbol{\beta}))$ described by the following Jacobian in the linear approximation:

$$\frac{\partial\boldsymbol{\beta}}{\partial\boldsymbol{\theta}} = \begin{pmatrix} 1-\kappa-\gamma_1 & -\gamma_2 \\ -\gamma_2 & 1-\kappa+\gamma_1 \end{pmatrix} \tag{1}$$

which includes shear $\gamma \equiv \gamma_1 + \mathrm{i}\gamma_2 = |\gamma|\mathrm{e}^{2\mathrm{i}\varphi}$ and convergence κ. These are in turn related to the deflection potential

$$\psi(\boldsymbol{\theta}) = \frac{1}{\pi}\int \mathrm{d}^2\theta'\,\kappa(\boldsymbol{\theta}')\,\ln|\boldsymbol{\theta}-\boldsymbol{\theta}'|\,, \tag{2}$$

via

$$\begin{aligned} \kappa(\boldsymbol{\theta}) &= \frac{1}{2}\nabla^2\psi(\boldsymbol{\theta}) \\ \gamma_1 &= \frac{1}{2}(\psi_{,11}-\psi_{,22}) \\ \gamma_2 &= \psi_{,12} \end{aligned} \tag{3}$$

and to the projected lens mass distribution via

$$\kappa(\boldsymbol{\theta}) = \frac{\Sigma(D_\mathrm{l}\boldsymbol{\theta})}{\Sigma_\mathrm{c}}. \tag{4}$$

Here we have used a critical surface density (geometric factor) defined as[9]

$$\Sigma_\mathrm{c} = \frac{c^2}{4\pi G}\,\frac{D_\mathrm{s}}{D_\mathrm{l}\,D_\mathrm{ls}} \tag{5}$$

in terms of the angular diameter distances to the source (D_s), lens (D_l), and between the two (D_ls).

The vast majority of the weak lensing measurements to date have focused on the measurement of shear (shape distortions) rather than convergence (magnification), and therefore require extremely accurate measurement of the shapes of source galaxies.

3 PSF CORRECTION

A complicating factor in lensing measurements is that in practice, the galaxy shape that is observed has not just been lensed; it has also passed through an atmosphere (for a ground-based telescope), telescope optics, and a detector. This results in a convolution of the intrinsic galaxy profile with the point-spread function, or PSF. In this paper, we define the PSF as including not just atmospheric blurring, optic, and detector effects, but also pixelisation (the 'effective PSF' or 'ePSF' in Bernstein & Jarvis 2002). Fortunately, the images of the stars provide a measurement, albeit a noisy one, of the PSF.

In order to measure the weak lensing shear, we must remove the effects of the PSF on the source galaxy shape. There are many methods of doing so; see Massey et al. (2007a) or Bridle et al. (2010) for summaries of the common methods of PSF correction. There are several types of bias that can arise when trying to extract the lensing shear using the PSF-corrected shapes (Hirata et al. 2004), for example:

[9] Eq. (5) is written in physical coordinates for simplicity; in comoving coordinates additional factors appear.

(i) *PSF dilution:* The PSF tends to round galaxy shapes. If this rounding is not fully accounted for, it leads to a multiplicative calibration bias that may depend on the galaxy profile, S/N, resolution, or PSF characteristics.

(ii) *Systematic shear:* If the PSF has some nonzero ellipticity, then imperfect removal of that ellipticity can manifest as a small ellipticity added to each galaxy shape. Since PSF shapes tend to have coherent correlations across the sky, this leads to a spurious systematics signal in the lensing measurement.

(iii) *Selection bias:* There are several types of selection bias. For example, for galaxies of a given apparent size, it may be easier to distinguish the more flattened ones from stars, and so the more flattened ones may be more likely than rounder ones to end up in a source galaxy sample. A selection bias that goes in the opposite direction is that some methods may have trouble extracting robust shapes for more flattened galaxies, thus selecting against them.

(iv) *Noise rectification bias:* For sparsely sampled realizations of an elliptical density distribution, the ellipticity tends to be over-estimated. This is an example of noise rectification bias, which is known to affect weak lensing measurements both in introducing spurious additive biases and affecting the calibration of the shears (Kaiser 2000; Bernstein & Jarvis 2002; Hirata et al. 2004). The details of how it affects shape measurements depends on the details of how the shape measurements and PSF correction are performed. For an example calculation of noise rectification bias as a function of detection significance, for methods that measure shapes using adaptive galaxy moments, see Hirata et al. (2004).

(v) *Population uncertainties:* Some methods of shape measurement rely on calibration factors that depend on the *intrinsic* properties of the galaxy population being studied, such as its ellipticity distribution. Since we only observe the ellipticities after the PSF and noise have been added, we are necessarily limited in how well we can infer the intrinsic properties of the sample. For some methods, e.g. as in Hirata et al. (2004), this results in the *shear responsivity uncertainty*. For other methods, such as Lensfit which uses a prior on the ellipticity distribution for Bayesian inference of galaxy shapes, the use of the wrong prior can result in an incorrect inference of the shear (Miller et al. 2007).

Because of the forms that these systematics take, shape measurement systematics have typically been quantified (Heymans et al. 2006; Massey et al. 2007a) using two numbers: a multiplicative calibration bias[10] m, and an additive calibration bias c, relating the estimated shear $\hat{\gamma}$ to the true one γ:

$$\hat{\gamma} - \gamma = m\gamma + c. \quad (6)$$

An ideal method would have $m = c = 0$ for all galaxy types, PSFs, and observing conditions (size of the galaxy relative to the PSF, and S/N). Unfortunately, even for existing methods that have m and c that average to nearly zero for some galaxy populations, m and c typically vary with all of these factors (Massey et al. 2007a; Bridle et al. 2010), so that in conditions other than the ones they were tested on, these biases may be significant.

It is worth explicitly contrasting the approaches to galaxy models that are commonly used for testing software used for weak lensing shear estimation. One common method is to use analytic formulae such as Sérsic profiles, either individually or as multi-component models with a bulge and disk. The clear advantage of this approach is that one is in principle only limited by computer processing power and storage space in how many simulations to generate. The disadvantage is that these models do not, in detail, represent galaxy profiles well. For example, spiral arms are completely unrepresented by such an approach, and higher redshift galaxies ($z \gtrsim 1$) are more likely to be highly irregular and therefore unrepresented. Massey et al. (2007b) and Zhang & Komatsu (2011) showed that there is no stable shape measurement algorithm on finite-resolution data that has a shear calibration factor that is independent of the galaxy population, because the shear operation inevitably couples the lower-order moments of a sheared galaxy to higher-order moments (which include not just the radial profile, but spiral arms, irregularity, etc.). A simulation containing simple models does not capture the higher-order moments of real galaxies, and so we do not expect that it will fully test for the (always present) dependence of shear calibration on the higher-order structure. Another example is that the single-component models lack ellipticity gradients (changes in the projected ellipticity and/or twists of the isophotes). These features are known to exist at a non-negligible level in real galaxies (e.g., Lauer 1985, Hao et al. 2006, Kormendy et al. 2009), and cause biases in shear estimation for most extant shape measurement methods (Bernstein 2010). Finally, pure-Sérsic simulations do not test for "underfitting" biases[11] in shear measurement methods that fit Sérsic profiles to galaxies.

Another approach is represented by the STEP2 simulations, which used shapelets decompositions of COSMOS galaxies (including the PSF, which was not removed). These simulations are therefore intrinsically limited by the cosmic variance in the COSMOS field. However, the clear advantage is that in principle, shapelets can (as an orthonormal basis set) represent *any* galaxy features. Unfortunately, due to the finite signal-to-noise of real data, it is necessary to truncate the shapelets expansion at some finite order. The consequence of this limitation has been documented in the literature (e.g., Melchior et al. 2010), and results in difficulty accurately representing galaxies with high Sérsic index, because of the need to represent both the strong inner cusp and the large-scale wings of the profile. As shown there, this modeling difficulty can cause $\sim$ 20 per cent biases when recovering the shear. Furthermore, the lower pre-seeing RMS galaxy ellipticity in the STEP2 simulations at faint magnitudes, $e_{\rm rms} = 0.20$ at $r = 26$ versus 0.35 at $r = 22$ (Massey et al. 2007a) might arise primarily from the fact that the shapelets expansion was limited to a lower order for the fainter galaxy sample, For a circular

[10] Massey et al. (2007a) also allowed for the possibility of a nonlinear response to shear, $\propto \gamma^2$.

[11] These are biases in an M-parameter fit to an image that arise when the true image has $N > M$ parameters, and some of the $N - M$ additional parameters are correlated with parameters of interest; see, e.g., Bernstein 2010.

shapelets basis, the restriction to lower order tends to give rounder galaxies[12]. Support for this statement comes from the fact that PSF-corrected COSMOS galaxy shapes using a non-shapelets based method (Leauthaud et al. 2007) have a roughly flat RMS ellipticity as a function of magnitude. Given that nearly all extant PSF-correction methods unfortunately have galaxy population-dependent (and ellipticity-dependent) shear calibrations, we cannot blindly use simulations that may not accurately represent some non-negligible part of the galaxy population to calibrate the shears coming from these methods to very high precision.

Finally, we consider the approach advocated here, using SHERA to represent realistic galaxies. The current limitation set by the cosmic variance in the COSMOS field is unfortunate, but we can ameliorate this problem in the future by using the *HST* archive to expand the set of galaxies that can be used as the basis for simulations, both to other ACS fields and to include images from other *HST* instruments. Also, since we are using realistic galaxies without modeling assumptions, we are free from concerns that some method of shape measurement might appear to perform unfairly well because the galaxies were constructed using the same set of models used for PSF correction. More generally, we do not have to worry that we have missed features of the galaxy population that are problematic for some or all methods of PSF correction. The results of Bridle et al. (2010), and others cited in Sec. 1, strongly suggest that if we want to precisely estimate the bias due to use of some particular shape measurement method in real data, we must include realistic galaxies and observing conditions. However, this conclusion does not undermine the utility of the STEP and GREAT simulations. For example, the GREAT simulations provide a very well-defined way to test the performance of shape measurement methods as a function of particular parameters (S/N, PSF size, galaxy radial profile) while keeping other parameters fixed. This test provides valuable insight into the failure modes of particular methods, facilitating method development, whereas SHERA effectively integrates over the parameters of the galaxy profile, PSF size, and other survey parameters to provide a good overall bias estimate, without necessarily revealing the details provided by the GREAT simulations.

4 DATA

In this section, we describe the space-based data used as inputs to the simulation pipeline, and the SDSS data that are being simulated as a test case.

4.1 COSMOS

The COSMOS *Hubble Space Telescope* (*HST*) Advanced Camera for Surveys (ACS) field (Koekemoer et al. 2007; Scoville et al. 2007a,b) is a contiguous 1.64 degrees^2 region centred at 10:00:28.6, +02:12:21.0 (J2000). Between October 2003 and June 2005 (*HST* cycles 12 and 13), the region was completely tiled by 575 adjacent and slightly overlapping pointings of the ACS Wide Field Channel. Images were taken through the wide F814W filter ("Broad I"). In this paper we use the 'unrotated' images (as opposed to North up) to avoid rotating the original frame of the PSF. By keeping the images in the default unrotated detector frame, they can be stacked to map out the observed PSF patterns. The raw images are corrected for charge transfer inefficiency (CTI) following Massey et al. (2010b). Image registration, geometric distortion, sky subtraction, cosmic ray rejection and the final combination of the dithered images are performed by the multidrizzle algorithm (Koekemoer et al. 2002). As described in Rhodes et al. (2007), the multidrizzle parameters have been chosen for precise galaxy shape measurement in the co-added images. In particular, a finer pixel scale of $0.03''$/pix was used for the final co-added images (7000×7000 pixels). The source catalogue used in this paper is constructed following the methodology outlined in Leauthaud et al. (2007) and then matched to an updated version (v1.7 dated from the 1$^{\rm st}$ of August 2009) of the COSMOS photometric redshift catalogue presented in Ilbert et al. (2009). For the purposes of this paper, the following cuts are then applied:

- $F814W < 22.5$: This cut allows us to start with a parent sample of galaxies that is deeper than what can be seen in SDSS, but still with very high S/N in the COSMOS images.
- MU_CLASS = 1: This requirement uses the relationship between the object magnitude and peak surface brightness to select galaxies, and to reject stars and junk objects such as residual cosmic rays (the exact definition of MU_CLASS can be found in Leauthaud et al. 2007).
- CLEAN = 1: As in Leauthaud et al. (2007), this cut is required to eliminate galaxies with defects due to very nearby bright stars, or other similar issues.
- GOOD_ZPHOT_SOURCE = 1: This cut requires that there be a good photometric redshift, which typically is equivalent to requiring that the galaxy not be located within the masked regions of the Subaru $BVIz$ imaging used for photometric redshifts, and that it have a successful match against an object in the Subaru imaging.

The first two cuts give an ideal parent sample of 33 517 galaxies, and the latter two cuts (which are necessary in practice for manipulating the images) reduce that to 30 225. Some of these galaxies are too faint to be detected in SDSS, and some are too small to be resolved given the size of the SDSS PSF. For each of these galaxies, an ideal postage-stamp size is estimated as

$$L(\text{pixels}) = 11\sqrt{(1.5r_{1/2})^2 + \left(\frac{1.2}{0.03 \times 2.35}\right)^2}. \quad (7)$$

This estimate uses the SExtractor[13] (Bertin & Arnouts 1996) FLUX_RADIUS (calculated with PHOT_FLUXFRAC= 0.5) as an estimate of the half-light radius $r_{1/2}$, and (in a Gaussian approximation, with $r_{1/2} \sim 0.7\sigma$) adds it in quadrature with an SDSS PSF of FWHM = $1.2''$, a typical value. The factor of 0.03 converts

[12] In practice, we also expect some contribution to this rounding from the fact that the ACS PSF was not removed from the COSMOS galaxies.

[13] `http://www.astromatic.net/software/sextractor`

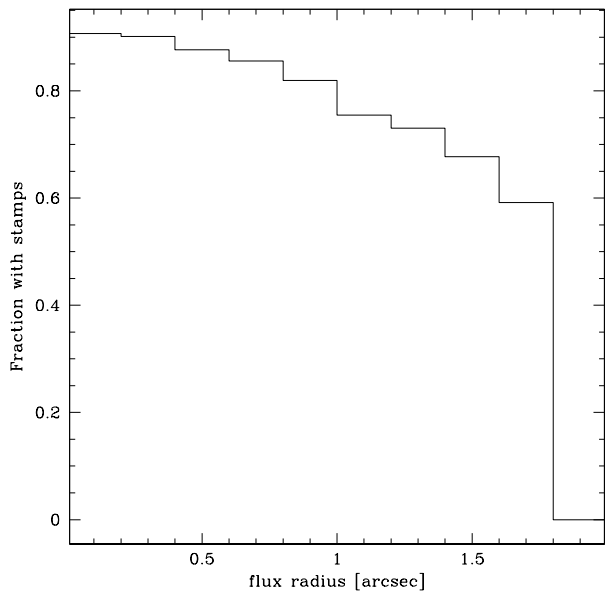

Figure 1. The fraction of galaxies in the parent sample of clean $F814W < 22.5$ galaxy detections for which a postage stamp was generated, as a function of the COSMOS SExtractor FLUX_RADIUS.

the FWHM in arcsec to the COSMOS pixel scale, and the 2.35 is required to express the typical SDSS 1.2″ PSF FWHM as a Gaussian σ. It then requires that the postage stamp go to more than $\pm 5\sigma$ in the predicted galaxy size after convolution with the target PSF.[14] If this postage stamp size causes the postage stamp to hit the CCD edge, then the galaxy is eliminated. Likewise, those galaxies for which the ideal postage stamp size exceeds $L = 1000$ pixels were eliminated (119 objects), resulting in an intrinsic upper limit in the values of FLUX_RADIUS for which postage stamps were generated. Consequently, the probability of a galaxy in our parent sample having a postage stamp is a weak function of the observed galaxy size, specifically the FLUX_RADIUS. This probability is shown in Fig. 1; when computing statistics of the sample, we must weight by the inverse of this curve to remove this artificial selection effect and obtain a fair galaxy sample.

After these cuts to ensure that the postage stamp can be generated, the sample for which there are postage stamps contains 26 113 galaxies.

4.2 SDSS

The SDSS (York et al. 2000) imaged roughly π steradians of the sky, and followed up approximately one million of the detected objects spectroscopically (Eisenstein et al. 2001; Richards et al. 2002; Strauss et al. 2002). The imaging was carried out by drift-scanning the sky in photometric conditions (Hogg et al. 2001; Ivezić et al. 2004), in five bands (*ugriz*) (Fukugita et al. 1996; Smith et al. 2002) using a specially-designed wide-field camera (Gunn et al. 1998). These imaging data were used to create the cluster and source catalogues that we use in this paper. All of the data were processed by completely automated pipelines that detect and measure photometric properties of objects, and astrometrically calibrate the data (Lupton et al. 2001; Pier et al. 2003; Tucker et al. 2006). The SDSS I/II imaging surveys were completed with a seventh data release (Abazajian et al. 2009), though this work will rely as well on an improved data reduction pipeline that was part of the eighth data release, from SDSS III (Aihara et al. 2011).

4.3 Shape catalogue

The catalogue of source galaxies with shape measurements that we are simulating in this work is described in Reyes et al. (2011, in prep.), and is an update of that originally described in Mandelbaum et al. (2005) with additional area and several technical improvements. This source sample has over 42 million galaxies from the SDSS imaging data with r-band model magnitude brighter than 21.8, with shape measurements obtained using the REGLENS pipeline, including PSF correction done via re-Gaussianization (Hirata & Seljak 2003) and with cuts designed to avoid various shear calibration biases. Among those cuts are a flux limit of $r < 21.8$, and the requirement that the PSF-corrected shape be measured in both r and i bands with sufficient resolution (to be defined more quantitatively later in this section).

Using the software developed in this work, we hope to more tightly constrain the shear calibration, including the full list of possible biases from Sec. 3, than was originally possible in Mandelbaum et al. (2005) (which had allowed for an overall 2σ shear calibration uncertainty of $[-5, +12]$ per cent for $r < 21$ galaxies, and $[-8, 18]$ per cent for $r > 21$ galaxies).

One of the technical difficulties that complicates any direct comparison of these shape measurements with those from the COSMOS catalogue is the definition of the shapes. Both the RRG method and re-Gaussianization define ellipticity in terms of a moment matrix $\mathbf{M}$ via

$$\begin{aligned} e_1 &= \frac{M_{xx} - M_{yy}}{M_{xx} + M_{yy}} \\ e_2 &= \frac{2M_{xy}}{M_{xx} + M_{yy}} , \end{aligned} \tag{8}$$

which translates to an ellipticity definition

$$|e| = \frac{1 - q_{\rm eff}^2}{1 + q_{\rm eff}^2} \tag{9}$$

for some effective minor-to-major axis ratio $q_{\rm eff} \equiv b_{\rm eff}/a_{\rm eff}$. However, the determination of the moment matrix $\mathbf{M}$, and therefore the e_1, e_2, and $q_{\rm eff}$, is done differently for the two methods.

In general, the definition of moments according to each method uses

$$M_{ij}^{(\rm method)} = \int I(\boldsymbol{x}) w_{\rm method}(\boldsymbol{x}) (\boldsymbol{x} - \boldsymbol{x}_0)_i (\boldsymbol{x} - \boldsymbol{x}_0)_j {\rm d}\boldsymbol{x}. \tag{10}$$

The RRG method, used to PSF-correct the COSMOS galaxy

[14] Note that FLUX_RADIUS is an azimuthally-averaged quantity. Thus, for highly flattened objects, we may be concerned that PSF convolution will cause them to become so large that they do not fit on the generated images. We test explicitly whether this is the case before using the resulting postage stamps.

shapes, defines second moments with a weight function

$$w_{\rm RRG}(\boldsymbol{x}) = \exp\left(-\frac{x^2+y^2}{r_w^2}\right), \quad (11)$$

where r_w is a galaxy size estimate calculated from the SExtractor detection area. Thus, this method uses a *circularly-weighted* moment with a fixed radius. In contrast, the re-Gaussianization method uses adaptive moments, which entails minimizing the integral

$$E = \frac{1}{2}\int \left| I(\boldsymbol{x}) - A\exp\left[-\frac{1}{2}(\boldsymbol{x}-\boldsymbol{x}_0)^T\mathbf{M}^{-1}(\boldsymbol{x}-\boldsymbol{x}_0)\right]\right|^2 {\rm d}^2\boldsymbol{x} \quad (12)$$

over the quantities $(A, \boldsymbol{x}_0, \mathbf{M})$. This procedure amounts to weighting by $w^{(\rm adapt)}(\boldsymbol{x})$ corresponding to the best-fitting *elliptical* Gaussian that represents the image itself, which in practice is determined iteratively.

Analytical calculations show that for an elliptical Gaussian profile, the difference between the circular vs. elliptical weight functions means that the two ellipticities $|e^{(\rm RRG)}|$ and $|e^{(\rm adapt)}|$ will be related as

$$|e^{(\rm adapt)}| = \frac{2|e^{(\rm RRG)}|}{1+|e^{(\rm RRG)}|}. \quad (13)$$

Furthermore, for non-Gaussian light profiles, $e^{(\rm adapt)}$ does not depend on any assumed radius whereas $e^{(\rm RRG)}$ does; more problematically, for a profile with fixed axis ratio, changing the profile from Gaussian to a more general profile with elliptical isophotes (e.g. Sérsic profiles) does not modify $|e^{(\rm adapt)}|$ whereas it does change $|e^{(\rm RRG)}|$. Finally, in the presence of ellipticity gradients with radius, the different way of choosing the effective radius of the weight function will result in different measured ellipticities. So, we cannot compare individual estimates of the galaxy shapes from the two PSF correction methods in any obviously model-independent way. We therefore conclude that the way forward is a simulation of the ground-based image using the high resolution COSMOS image, in order to directly test the accuracy of shear recovery.

For the purpose of this work, we define the 'resolution factor' R_2 using the trace of the adaptive moment matrices,

$$T = M_{xx} + M_{yy} \quad (14)$$

where $T^{(P)}$ and $T^{(I)}$ are the traces for the PSF and for the PSF-convolved galaxy image, respectively. Then the resolution factor is

$$R_2 = 1 - \frac{T^{(P)}}{T^{(I)}}\ , \quad (15)$$

which approaches 1 in the limit that the galaxy is perfectly resolved, and 0 in the limit that it is completely unresolved. Our requirement on the resolution factor is $R_2 > 1/3$. In the limit of Gaussian PSF and galaxy with standard deviations $\sigma_{\rm gal}$ and $\sigma_{\rm PSF}$, respectively, this resolution factor cut corresponds to $\sigma_{\rm gal} > \sigma_{\rm PSF}/\sqrt{2}$.

5 SIMULATION METHODOLOGY

In this section, we discuss the principles behind simulations of lower-resolution (ground-based) data from higher-resolution (space-based) data. First, we define some notation.

We assume that a galaxy is described by an intrinsic unknown surface brightness function $f(\mathbf{x})$ as a function of angular position $\mathbf{x}$. We are given a high-resolution image (COSMOS) with some effective PSF $G_1(\mathbf{x})$, i.e. the observed surface brightness is

$$I_1(\mathbf{x}) = [f \star G_1](\mathbf{x}) = \int f(\mathbf{x}')G_1(\mathbf{x}-\mathbf{x}')\,{\rm d}^2\mathbf{x}'. \quad (16)$$

We would like to generate a low-resolution image I_2 (corresponding to what would be observed by some ground-based telescope with PSF G_2),

$$I_2(\mathbf{x}) = [f \star G_2](\mathbf{x}) = \int f(\mathbf{x}')G_2(\mathbf{x}-\mathbf{x}')\,{\rm d}^2\mathbf{x}'. \quad (17)$$

While this equation may initially appear to represent a trivial PSF-matching process (Sec. 5.1), there is a complicating factor that arises if we want to represent a sheared image (Sec. 5.2), since shearing and convolution by the space-based PSF do not commute.

5.1 PSF matching

First, we consider the case in which we simply wish to generate a low-resolution image without any added shear. In that case, the task of generating a low-resolution image I_2 is simply a matter of PSF-matching. The simplest model-independent way to do this is to work in Fourier space[15]. In that case, the convolutions with the PSF are multiplications:

$$\tilde{I}_1(\mathbf{k}) = \tilde{f}(\mathbf{k})\tilde{G}_1(\mathbf{k}) \quad (18)$$

and likewise for the low resolution image $\tilde{I}_2$.

In that case, once we have a Fourier-space image $\tilde{I}_1$, original PSF $\tilde{G}_1$ and target PSF $\tilde{G}_2$, we can simply generate the low-resolution image via

$$\tilde{I}_2 = \left(\frac{\tilde{G}_2}{\tilde{G}_1}\right)\tilde{I}_1. \quad (19)$$

Naturally, we must place some conditions on the low- and high-resolution PSFs in order to carry out this PSF matching. As a rule, PSFs are band-limited at some wavenumber k_c above which there is essentially no power (this corresponds to the small scales below which there is no information about the galaxy profile). By definition, the PSFs in high and low resolution data tend to satisfy $|\tilde{G}_1| > |\tilde{G}_2|$ at all wavenumbers k, with the band limit $k_{c,1} > k_{c,2}$; for an example of how this relation is satisfied for typical COSMOS and SDSS data, see Fig. 2, and the corresponding real-space PSF images in Fig. 3. In fact, this inequality is a requirement for numerically stable and model-independent PSF-matching; if it is not satisfied, then the operation in Eq. (19) corresponds to deconvolution for at least some wavenumbers, which will lead to undesired image properties such as ringing. This deconvolution can be done in the context of model-fitting methods; however, the meaning of the small-scale power recovered in the process of such a deconvolution is unclear (Bernstein 2010).

[15] We indicate Fourier-space quantities with a tilde, and the distances in pixels in real and Fourier space are $\boldsymbol{x}$ and $\boldsymbol{k}$, respectively.

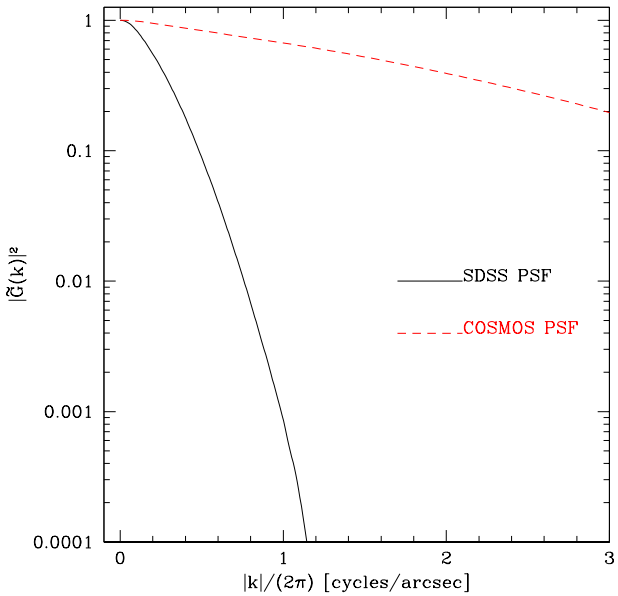

Figure 2. An example of the relevant scales for the PSF in SDSS and COSMOS at a randomly-selected point in the COSMOS field. The plotted quantity is the azimuthally-averaged PSF power $|\tilde{G}|^2$, as a function of wavenumber. As shown, the band limit of the SDSS data is on scales where the Fourier transform of the COSMOS PSF is still close to 1.

5.2 Introducing a shear

Now, we consider the less trivial case where we want to simulate a ground-based image with an added shear, for the purpose of testing PSF correction. We denote this sheared ground-based image $I_2^{(\gamma)}(\mathbf{x})$ to distinguish it from the unsheared ground-based image $I_2(\mathbf{x})$ considered in the previous subsection.

To define the problem more clearly, we imagine a Jacobian matrix $\mathbf{J}$ that transforms the observed (post-shear) coordinates $\mathbf{x}_\mathrm{o}$ to the intrinsic (pre-shear) coordinates $\mathbf{x}_\mathrm{i}$ on a galaxy:

$$\mathbf{x}_\mathrm{i} = \mathbf{J}\mathbf{x}_\mathrm{o}. \tag{20}$$

The Jacobian $\mathbf{J}$ is thus a 2×2 matrix. Usually $\mathbf{J}$ will be close to the identity; indeed, to first order in the shear, $\mathbf{J}$ is simply given by Eq. (1). We will denote the singular values of $\mathbf{J}$ by $S_\pm$, with $S_- \leqslant S_+$, and $\det \mathbf{J} = S_- S_+$. If $\mathbf{J}$ is symmetric, then $S_\pm$ are also the eigenvalues.

We then have a sheared galaxy image

$$f_\mathrm{o}(\mathbf{x}_\mathrm{o}) = f(\mathbf{J}\mathbf{x}_\mathrm{o}), \tag{21}$$

and the observed sheared image is

$$I_2^{(\gamma)}(\mathbf{x}_\mathrm{o}) = [f_\mathrm{o} \star G_2](\mathbf{x}_\mathrm{o}) = \int f(\mathbf{J}\mathbf{x}')G_2(\mathbf{x}_\mathrm{o} - \mathbf{x}')\,\mathrm{d}^2\mathbf{x}'. \tag{22}$$

It is assumed that the S/N of the input images is large enough that the noise is negligible. (Clearly the output image may be made to have arbitrary levels of noise by adding noise at the end.) For the situation considered here, we thus limit ourselves to relatively bright detections in COSMOS ($S/N \gtrsim 50$). In Sec. 8.5, we demonstrate the effects of this low level of noise in the input images on the simulated images, given that it is sheared and therefore could contribute to an estimated shear. We defer the development of a formalism to account for non-negligible noise levels in the input high-resolution data to future work that may use lower S/N space-based data.

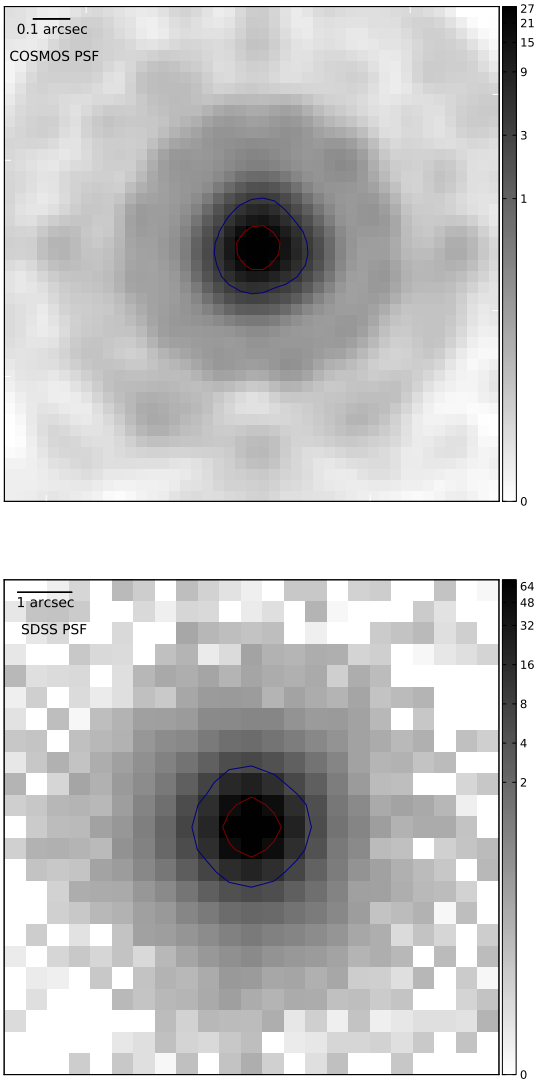

Figure 3. *Top:* Real-space image of the Tiny Tim COSMOS PSF for which the azimuthally averaged Fourier space power was shown in Fig. 2. The image is shown on a logarithmic stretch, in order to display the diffraction rings. Contours are shown for a flux level equal to 0.5 and 0.1 times the maximum flux level. *Bottom:* Same as top, for the SDSS PSF; the low-level patterns in the outer regions are due to a small amount of noise in the PSF model.

We assume that the PSFs G_1 and G_2 satisfy the following band-limiting constraints: first, that $|\tilde{G}_2(\mathbf{k})| = 0$ (or at least is negligible) for $|\mathbf{k}| > k_c$ for some k_c (the band limit); and second, that $|\tilde{G}_1(\mathbf{k})|$ is nonzero (and in practice we assume it is far from zero, e.g. $\gtrsim 0.5$) for $|\mathbf{k}| < k_d$ for some k_d. We impose the assumption that

$$k_c < S_- k_d, \tag{23}$$

which in practices amounts to requiring a significant range of scales on which the ground-based PSF erases all information that is still resolvable in the space-based images.

While the PSF-matching problem can be simply formulated as trying to take $I_1(\mathbf{x})$ and obtain $I_2(\mathbf{x})$, the case where we want to introduce a shear for testing purposes (a simulated gravitational shear, which changes the galaxy image *before* the imposition of the PSF) instead requires us to infer $I_2^{(\gamma)}(\mathbf{x}_\mathrm{o})$.

The principle behind the solution is to attempt a partial deconvolution of I_1. We now define a filter $T(\mathbf{x})$ that has a Fourier transform satisfying

$$\tilde{T}(\mathbf{k}) = \frac{1}{\tilde{G}_1(\mathbf{k})} \text{ for } |\mathbf{k}| < k_d. \tag{24}$$

(Here we have used our band-limiting condition on G_1.) For $|\mathbf{k}| \geqslant k_d$ an arbitrary choice of $\tilde{T}(\mathbf{k})$ may be made, e.g. it may be taken to decrease smoothly to zero so that the real-space function $T(\mathbf{x})$ does not have tails at large radii.

Then we define the *pseudo-deconvolved* image $P(\mathbf{x})$ by

$$P(\mathbf{x}) = [I_1 \star T](\mathbf{x}) = \int I_1(\mathbf{x}')T(\mathbf{x}-\mathbf{x}')\,\mathrm{d}^2\mathbf{x}', \tag{25}$$

or in Fourier space,

$$\tilde{P}(\mathbf{k}) = \tilde{I}_1(\mathbf{k})\tilde{T}(\mathbf{k}) = \tilde{f}(\mathbf{k})\tilde{G}_1(\mathbf{k})\tilde{T}(\mathbf{k}), \tag{26}$$

so that $\tilde{P}(\mathbf{k}) = \tilde{f}(\mathbf{k})$ for $|\mathbf{k}| < k_d$.

Our second step is to shear the pseudo-deconvolved image, i.e. we create

$$P_\mathrm{o}(\mathbf{x}_\mathrm{o}) = P(\mathbf{J}\mathbf{x}_\mathrm{o}). \tag{27}$$

The Fourier transform is given by the usual rule for the transform of a quantity with a linear shear,

$$\tilde{P}_\mathrm{o}(\mathbf{k}_\mathrm{o}) = \frac{1}{|\det \mathbf{J}|}\tilde{P}(\mathbf{J}^{T\,-1}\mathbf{k}_\mathrm{o}). \tag{28}$$

The singular values of $\mathbf{J}^{T\,-1}$ are $S_\pm^{-1}$. Therefore, we see that if $|\mathbf{k}_\mathrm{o}| < k_c$, then:

$$|\mathbf{J}^{T\,-1}\mathbf{k}_\mathrm{o}| \leqslant S_-^{-1}|\mathbf{k}_\mathrm{o}| < S_-^{-1}k_c < k_d. \tag{29}$$

Therefore, $\tilde{P}_\mathrm{o}(\mathbf{k}_\mathrm{o}) = \tilde{f}_\mathrm{o}(\mathbf{k}_\mathrm{o})$ for $|\mathbf{k}_\mathrm{o}| < k_c$.

Finally, we convolve P_o with the target low-resolution PSF G_2 to get

$$H(\mathbf{x}_\mathrm{o}) = [P_\mathrm{o} \star G_2](\mathbf{x}_\mathrm{o}) = \int P_\mathrm{o}(\mathbf{J}\mathbf{x}')G_2(\mathbf{x}_\mathrm{o}-\mathbf{x}')\,\mathrm{d}^2\mathbf{x}'. \tag{30}$$

In this case, we have

$$\tilde{H}(\mathbf{k}_\mathrm{o}) = \tilde{P}_\mathrm{o}(\mathbf{k}_\mathrm{o})\tilde{G}_2(\mathbf{k}_\mathrm{o}). \tag{31}$$

There are now two cases: $|\mathbf{k}_\mathrm{o}|$ is either (i) $< k_c$ or (ii) $\geqslant k_c$. We consider each of these:

- If $|\mathbf{k}_\mathrm{o}| < k_c$, then $\tilde{P}_\mathrm{o}(\mathbf{k}_\mathrm{o}) = \tilde{f}_\mathrm{o}(\mathbf{k}_\mathrm{o})$ so $\tilde{H}(\mathbf{k}_\mathrm{o}) = \tilde{I}_2^{(\gamma)}(\mathbf{k}_\mathrm{o})$.
- If $|\mathbf{k}_\mathrm{o}| \geqslant k_c$, then $\tilde{G}_2(\mathbf{k}_\mathrm{o}) = 0$ so $\tilde{H}(\mathbf{k}_\mathrm{o}) = \tilde{I}_2^{(\gamma)}(\mathbf{k}_\mathrm{o}) = 0$.

In either case, we have $\tilde{H}(\mathbf{k}_\mathrm{o}) = \tilde{I}_2^{(\gamma)}(\mathbf{k}_\mathrm{o})$, so it follows that $H(\mathbf{x}_\mathrm{o}) = I_2^{(\gamma)}(\mathbf{x}_\mathrm{o})$. Therefore, the function H that we have constructed is exactly the sheared image that would be observed with the low-resolution telescope.

5.3 Other observational issues

To demonstrate that the PSF-matching is accurate, we will determine the target PSF and noise level using the observing conditions at the position of the COSMOS galaxy in the SDSS imaging. This procedure will allow us to compare the simulations with the real SDSS imaging in the COSMOS field, as a basic test of the SHERA code. Likewise, we will use these simulations to determine the shear calibration bias, as a demonstration of the method. However, in order to make a fair test of the shear calibration of the entire SDSS shear catalogue, it would be necessary to draw random points from within the SDSS area and use the observing conditions from those points. The difference between these two approaches would not be significant if the quality of the SDSS imaging in the COSMOS field was representative, but as discussed in Appendix A, this is not the case.

Also, in order to fairly test the shear calibration, we must impose any selection criteria from the real data on the simulations. This will also allow for a test of selection biases, since the input galaxy sample is a fair sample of all galaxies brighter than some flux limit ($F814W < 22.5$) that is deeper than the SDSS flux limit in the single epoch images ($r < 21.8$).

Finally, one limitation of these COSMOS images that we use as the basis for our simulations is that they only are in $F814W$ (broad I). The existence of colour gradients means that the galaxies would look morphologically different in other passbands, and the effect is probably the strongest for galaxies with a reasonable-sized bulge and disk, for which the bulge is more prominent in red bands and the disk in blue bands. However, since most lensing analyses use r or I for shape measurement, this does not represent a significant limitation (Voigt et al. 2011). It is an argument, however, for using another field with multi-band data, provided that (a) the CTI effects (see section 4.1) are well-understood and corrected for properly, and (b) the field was chosen in some fair way (e.g., it is not a galaxy cluster field, which would have an atypical morphology distribution).

For our purposes in SDSS, we can use simulations with a fair distribution of observational conditions to precisely determine the i-band shear calibration. Since our science analyses use averaged r and i band shapes, we can then use the data itself to determine the ratio of the measured signal to that with just i band. The measurements in r and i are highly correlated because the shape noise is the same, so this allows the shear calibration for the actual science analyses to be determined very precisely.

6 IMAGE PREPARATION

Before we can actually carry out the image simulations, there are a number of steps that must be done to process the galaxy postage stamp images described in Section 4.1. These steps have been carried out already for the images that are being publicly released[16]. Thus, these newly released images differ from the already-public version 2 COSMOS images in that they are restricted to a bright subsample of galaxies,

[16] `http://irsa.ipac.caltech.edu/data/COSMOS/images/galaxy_postage_stamps/`

they have a smaller post-processing pixel scale (0.03"), they include the pixel-based CTI correction, and include the post-processing described in the remainder of this section.

6.1 Catalogue of galaxy properties

We have used the COSMOS data to prepare a number of inputs that can be used for simulations of SDSS i-band images.

First, we need a total galaxy flux in i band, whereas the COSMOS images are in $F814W$. A significant fraction of the galaxies that constitute our parent sample are detected in SDSS, and therefore have measurements of the i-band flux. However, these measurements are far noisier than the flux measurements from the COSMOS data, so we will use the COSMOS $F814W$ fluxes to determine the normalization of the flux in the simulated images.[17] We begin with the reported SExtractor MAG_AUTO magnitudes in $F814W$, which we correct for galactic extinction using the dust maps from Schlegel et al. (1998) and the extinction-to-reddening ratios from Stoughton et al. (2002). These magnitudes are designed to precisely determine the total magnitudes for galaxies, similar to Kron magnitudes (Kron 1980), and are superior to aperture magnitudes in recovering all the galaxy flux.

In order to account for slight differences in the two filters, we then compare the extinction-corrected COSMOS MAG_AUTO and SDSS model magnitudes for reasonably bright galaxies ($i < 20$), and determine a mean offset of 0.03 mag, $i = F804W - 0.03$. This mean offset is then subtracted from the $F814W$ magnitudes for all galaxies in the parent sample.

6.2 Postage stamp preparation

There are several types of processing that must be done to the original CTI-corrected galaxy postage stamps before using them as inputs to the simulations. For this purpose, we use SExtractor (Bertin & Arnouts 1996) v2.5.0. First, we run SExtractor with the COSMOS multidrizzle weight map for each postage stamp, instructing it to subtract off a flat background level equivalent to the residual background after the original multidrizzle processing was completed. We do not allow it to carry out its own sky determination because the size of the postage stamps is not sufficient for it to do so without being unduly influenced by the light of the galaxies in the postage stamp.

The results of this step provide us with a list of detected objects in the postage stamp. Ideally, if deblending is properly done, then one of those (our target galaxy) will be at the centre of the postage stamp. We use the SExtractor output segmentation image to identify all pixels belonging to objects other than the target galaxy, and replace those pixels with a noise field having the same noise characteristics as the rest of the postage stamp (including overall noise amplitude as well as pixel-to-pixel correlations). The number of masked objects is < 18 (< 60) for 50 (95) per cent of target galaxies, resulting in 0.9 (6) per cent of the pixels being masked; the majority of the masked objects are quite small and faint, with some appearing to be misidentification of the correlated noise as actual objects. This object masking procedure is dependent upon SExtractor correctly identifying all pixels belonging to other objects; it is not fully successful with some very bright objects, leaving a halo of pixels containing a low, but visually noticable, level of light surrounding the masked regions. Fortunately the incidence of such cases is low. These processed postage stamps are included with the code and data release.

While carrying out this procedure, we compute additional statistics for each postage stamp, including (a) the distance of the nearest object to the postage stamp centre (which we require to be $\leqslant 5$ pixels, after visual inspection of cases failing this cut suggested that those cases suffered from poor deblending), and (b) various noise statistics such as the median and the mean pixel value for those pixels not included in objects (which can differ significantly if there is some very large bright object in the postage stamp that did not get properly masked). Imposing cuts based on these statistics reduces the size of our sample from 26 113 to 25 527 postage stamps, a decrease in sample size of 2.2 per cent.

If the masked objects are sufficiently close to the central galaxy, then in the SDSS it will not be possible to distinguish between them. This fact will allow us to quantify the level of undeblended projections in our shape catalogue: we identify those cases for which the apparent size of the galaxy in the SDSS is significantly larger than its counterpart in the PSF-matched images from COSMOS.

6.3 COSMOS PSF estimation

In order to remove the effects of the COSMOS PSF, we must determine the COSMOS PSF at the galaxy position. We follow the same procedure as in Leauthaud et al. (2007) and Massey et al. (2007a), who use PSF models from a modification of version 6.3 of the Tiny Tim ray-tracing program[18]. These models represent PSFs for different primary/secondary separation, since that separation is the main determinant of the PSF ellipticity. They are known to be a bit too small because they neglect the 'red halo' that enlarges real *HST* PSFs at long wavelengths (Sirianni et al. 1998), possibly due to backscattering off the front surface of the CCD. We quantify whether the deviation between these models and the real stellar images represents a problem for using the models to simulate ground-based data in Sec. 8.4.

Our procedure is to use the previous determination (Leauthaud et al. 2007) of the primary/secondary separation for each exposure based on the ellipticity of ~ 20 bright stars, then to use that particular Tiny Tim model extrapolated to the CCD (x, y) position of each galaxy. The estimated Tiny Tim PSF for each galaxy position is included with the data release associated with this work.

6.4 Determination of target imaging properties

In this section, we describe what information must be specified about imaging conditions in the data that is to be sim-

[17] If we use the SDSS magnitudes, then we include noise in the measurement twice, since the SDSS magnitude measurements are noisy due to the sky noise that we then put into the simulations.

[18] `http://www.stsci.edu/software/tinytim/`

ulated. Here, we restrict ourselves to a general discussion; however, for the purpose of testing and demonstrating the code, we attempt to simulate the SDSS data in the COSMOS field. Appendix A contains details of exactly what SDSS pipeline outputs are used.

PSF: The desired PSF for the simulated data must be provided as a postage-stamp image. It should be the desired PSF including the pixel response function; e.g., if a Gaussian PSF is of interest as a test case, the Gaussian should be integrated within pixels, rather than sampled at the pixel centres.

Photometric calibration: The most basic case would be to simulate data using the $F814W$ magnitudes. To do so, the code requires the total flux normalization in counts, as determined from the COSMOS total galaxy magnitude and the flux normalization for the ground-based survey of interest.

Noise level: The default noise model is a spatially constant, uncorrelated Gaussian random field. For most ground-based surveys, the sky level is sufficiently high that the Poisson noise due to the sky is effectively Gaussian; and most galaxies used for weak lensing are sufficiently faint that the sky noise dominates over the noise due to the galaxy flux. Thus, the code simply requires a single noise variance to work in this basic mode. However, it also allows the choice of Poisson noise, and the user may optionally input a gain in order to also add the noise due to the galaxy flux (important for relatively bright galaxies). Future versions of the code may allow the user to simulate a correlated noise field with a user-defined noise power spectrum, which will be important for assessing the impact of correlated noise on shear estimation.

The simulated postage stamps have a sky level of zero. Any constant or varying sky should be added by the user after running SHERA.

7 IMPLEMENTATION

For compatibility with many common astronomical image manipulation packages, we have implemented this simulation method in IDL. The data release includes a detailed description of the code options; here, we limit ourselves to a basic description of how the code carries out the procedure from Sec. 5.

The SHERA code operates on a set of input postage stamps: the original COSMOS image and PSF, and a target PSF to which we want to match. The manipulation of the images to create the simulated galaxies is performed using double precision arithmetic.

The first step in the image manipulation is to change the sizes of the input postage stamps of the COSMOS galaxy, COSMOS PSF, and target PSF due to several considerations. When doing the Fourier space manipulations, it is convenient to have the ratio of the COSMOS and the target PSF postage stamp sizes be equal to the ratio of the target and COSMOS pixel sizes, which is $R_{\rm pix} = 0.396''/0.03''$ in the case of SDSS simulations (however, the code allows for nearly arbitrary choice of target pixel size, such that $R_{\rm pix} > 1$). Likewise, it will be most convenient when working in Fourier space if the COSMOS PSF and COSMOS galaxy postage stamp sizes are equal.

Thus, we begin by padding the arrays until they achieve the appropriate size ratios. While the default is to pad with zeros, we also provide the option of padding with a realistic COSMOS noise field. Once we have a target PSF postage stamp of size $N_{\rm T} \times N_{\rm T}$ and COSMOS galaxy and PSF postage stamps of size $N_{\rm C} \times N_{\rm C}$, with $N_{\rm C} = R_{\rm pix} N_{\rm T}$, we can proceed with the analysis. To begin, we renormalize the flux in the PSF postage stamps so that the sum of the flux in all pixels is 1.

In the description that follows, we denote the observed galaxy images using I (with subscript C for their image in COSMOS and T for the simulation of the target dataset), and PSFs using G (again with subscripts to indicate which PSF). Thus the images we begin with are $I_{\rm C}$, $G_{\rm C}$, and the target PSF $G_{\rm T}$. All three images are Fourier-transformed using the IDL routine `fft`, after which we multiply them by $N_{\rm C}^2$ or $N_{\rm T}^2$ for proper normalization. The result of the Fourier transform is a double-precision complex array with the same dimensions as the original.[19]

With the Fourier-space COSMOS PSF $\tilde{G}_{\rm C}$, we can now construct the pseudo-deconvolution kernel $\tilde{T}(\boldsymbol{k})$. Unlike a pure deconvolution kernel, $1/\tilde{G}_{\rm C}$, $\tilde{T}$ has an additional factor that avoids division by small numbers (i.e., where the COSMOS PSF has erased most information). We define this factor as

$$\tilde{Y}(\boldsymbol{k}) = \frac{1}{1 + |0.5/\tilde{G}_{\rm C}(\boldsymbol{k})|^{20}} \tag{32}$$

and thus $\tilde{T}$ by

$$\tilde{T}(\boldsymbol{k}) = \frac{\tilde{Y}(\boldsymbol{k})}{\tilde{G}_{\rm C}(\boldsymbol{k})}. \tag{33}$$

The $\tilde{Y}$ factor has been chosen to be very close to 1 for all scales where $|\tilde{G}_{\rm C}| \gtrsim 0.5$, and zero when $|\tilde{G}_{\rm C}| \lesssim 0.5$, with a smooth and rapid transition between these two regimes. Thus, it approximates a pure deconvolution at wavenumbers where such an approach is possible, and removes all power at smaller scales. In practice, comparison with Fig. 2 demonstrates that this kernel gives a pure deconvolution for all scales within a factor of 2 of the SDSS band limit.

The pseudo-deconvolved image (Eq. 26) can then be formed directly by multiplication of the elements of the two arrays at a given $\boldsymbol{k}$, using

$$\tilde{P}(\boldsymbol{k}) = \tilde{T}(\boldsymbol{k})\, \tilde{I}_{\rm C}(\boldsymbol{k}). \tag{34}$$

The PSF for this pseudo-deconvolved image is simply Eq. (32). Examination of these pseudo-deconvolved images in real-space suggests that they very frequently include some ringing, always at higher wavenumbers (smaller scales) than the band limit of any reasonable ground-based PSF. In practice this ringing is not relevant, since we do not work explicitly with the real-space pseudo-deconvolved images, and the step of convolving to match a ground-based PSF will remove the ringing.

At this stage, in order to reduce the effects of shape noise, we also define a 90 degree rotated galaxy image. Since

[19] While this resulting array would seem to have twice as much information as the original real-space arrays, in fact the real part of the result is even and the imaginary part is odd, so the amount of information is preserved.

we would like this image to be rotated before shearing or applying the target PSF, we rotate $\tilde{P}$ by 90 degrees about its central pixel to create $\tilde{P}^{(\rm rot)}$, and note that its effective PSF is the 90 degree rotation of Eq. (32).

The next step is to shear both $\tilde{P}$ and $\tilde{P}^{(\rm rot)}$. As described in Section 5, the shearing can be carried out simply in Fourier space using Eq. (28). We take advantage of the fact that the coordinates before and after shearing are linearly related to each other, and use the IDL routine `poly_2d` that is designed to perform polynomial warping of images with various interpolation methods. For the level of accuracy that we wish to achieve, we require the most precise (and time-intensive) interpolation allowed by that routine, cubic interpolation (Park & Schowengerdt 1983). This interpolation method approximates sinc interpolation, which is in principle exact if the image is Nyquist sampled. Instead of the sinc function, this routine uses cubic polynomials to make a function that is very similar, and that goes to zero (and has a derivative that goes to zero) at the edge of the window used for the interpolation. Since the arrays we want to shear are complex, we separately interpolate the norm and phase using this routine in order to reconstruct the sheared and pseudo-deconvolved images $\tilde{P}^{(\gamma)}$ and $\tilde{P}^{(\rm rot,\gamma)}$. In Sec. 8.1, we will present tests demonstrating that the interpolation routine we have used is sufficiently accurate for our purposes.

The final Fourier-space manipulation is to match the desired target PSF by constructing a kernel $\tilde{K}_{\rm T}$, or $\tilde{K}_{\rm T}^{(\rm rot)}$ for the 90 degree rotated image. To do this, we must divide the target PSF $\tilde{G}_{\rm T}$ by the effective PSF for the pseudo-deconvolved image (Eq. 32 or its 90 degree rotation). Once we have the matching kernel, the PSF-matching is then performed in Fourier space via multiplication of each element of $\tilde{P}^{(\gamma)}$ and $\tilde{P}^{(\rm rot,\gamma)}$ by the corresponding element of $\tilde{K}_{\rm T}$:

$$\tilde{I}_{\rm T}^{(\gamma)}(\boldsymbol{k}) = \tilde{P}^{(\gamma)}(\boldsymbol{k}) \times \tilde{K}_{\rm T}(\boldsymbol{k}) \tag{35}$$

and

$$\tilde{I}_{\rm T}^{(\rm rot,\gamma)}(\boldsymbol{k}) = \tilde{P}^{(\rm rot,\gamma)}(\boldsymbol{k}) \times \tilde{K}_{\rm T}^{(\rm rot)}(\boldsymbol{k}). \tag{36}$$

The transformation to real space is again carried out using `fft`. The real part of the resulting double-precision complex array is taken (in practice, the imaginary part, which should be precisely zero, is very small but nonzero due to negligibly small numerical inaccuracies). To achieve the target pixel scale, these images are resampled, which requires interpolation since the ratio of the pixel sizes is not necessarily an integer. For this purpose, we use the IDL routine `congrid` with cubic interpolation (the same interpolation used for the shearing, which approximates a sinc function). The Fourier-space PSF-matching procedure implicitly accounts for the different pixel response functions, which is why we resample rather than rebinning the images.

At this point, the total number of counts in the image is renormalized, and noise is added as desired. The total processing time per typical galaxy is approximately 1 second. For the purpose of our basic testing, we save four images per galaxy: the original orientation and the 90 degree rotated orientation, both before adding noise and after adding noise. For the purpose of the discussion that follows, we will refer to these as 'noiseless' (ignoring the low level of noise from the original COSMOS data) and 'noisy,' respectively.

An example of how this processing works for one particular COSMOS galaxy is shown in Fig. 4, which shows the original COSMOS image (with some fine structure), and the degraded SDSS image without and with a gravitational shear of $\gamma_1 = 0.1$, i.e. along the horizontal axis.

8 TECHNICAL VALIDATION OF SHERA

This section includes the results of several tests of the technical aspects of SHERA, to demonstrate that the procedure outlined in Sec. 7 works as intended.

8.1 Accuracy of interpolation

While most of the mathematical operations carried out by SHERA are simple and easy to carry out to extremely high accuracy (e.g., a Fourier transform), two of the operations are non-trivial because they involve interpolations. As described in Sec. 7, we use the IDL cubic interpolation routine both for shearing the pseudo-deconvolved images, and for resampling the PSF-matched images to the target pixel scale.

Here we present the results of tests that demonstrate that the IDL cubic interpolation routine is sufficiently accurate for both shearing and resampling. While we carried out numerous tests of the pipeline using both real galaxies and analytic models, here we focus on tests that use the real COSMOS galaxies, under the assumption that they provide a more stringent test than analytic galaxy and PSF profiles.

The first test is of the shearing of the pseudo-deconvolved image. In principle, we could carry out this test by transforming the pseudo-deconvolved image to real-space both before and after shearing, and then comparing the observed adaptive moment matrices. Since there is no PSF in these images, we can simply check that the moments transform under shear according to equation (2-13) of Bernstein & Jarvis (2002). However, as stated in Sec. 7, the pseudo-deconvolution leads to ringing in real-space. The ringing is relatively high frequency and therefore difficult to accurately interpolate, which might lead us to conclude that our shearing is not very accurate. However, this ringing does not affect the accuracy of the shearing on the final ground-based image since convolving with the ground-based PSF will eliminate the ringing. Thus, we restrict our tests of the pseudo-deconvolved images to the Fourier-space images used for the actual shearing, and check that the Fourier counterpart of equation (2-13) from Bernstein & Jarvis (2002) is satisfied.

For this test, we use a random 5 per cent of the COSMOS images, and apply a shear $(\gamma_1, \gamma_2) = (0.02, 0)$ before matching to SDSS. We do not add noise to the images, in order to allow for the highest possible precision in these tests. The motivation behind applying zero shear in one component is that it allows us to test that shearing one component does not lead somehow to spurious shearing in the component that we do not intend to shear. For each galaxy, we compute the adaptive moments of the pseudo-deconvolved Fourier space image before shearing (e_1, e_2) and after shearing $(e_1^{(\gamma)}, e_2^{(\gamma)})$. We then compare the latter with the expected ellipticities $(e_{1,\rm exp}^{(\gamma)}, e_{2,\rm exp}^{(\gamma)})$, to get the error in the observed shear $\Delta\gamma_i = e_i^{(\gamma)} - e_{i,\rm exp}^{(\gamma)}$ for $i = 1, 2$. We can use the values for this random subsample of the COSMOS galaxies

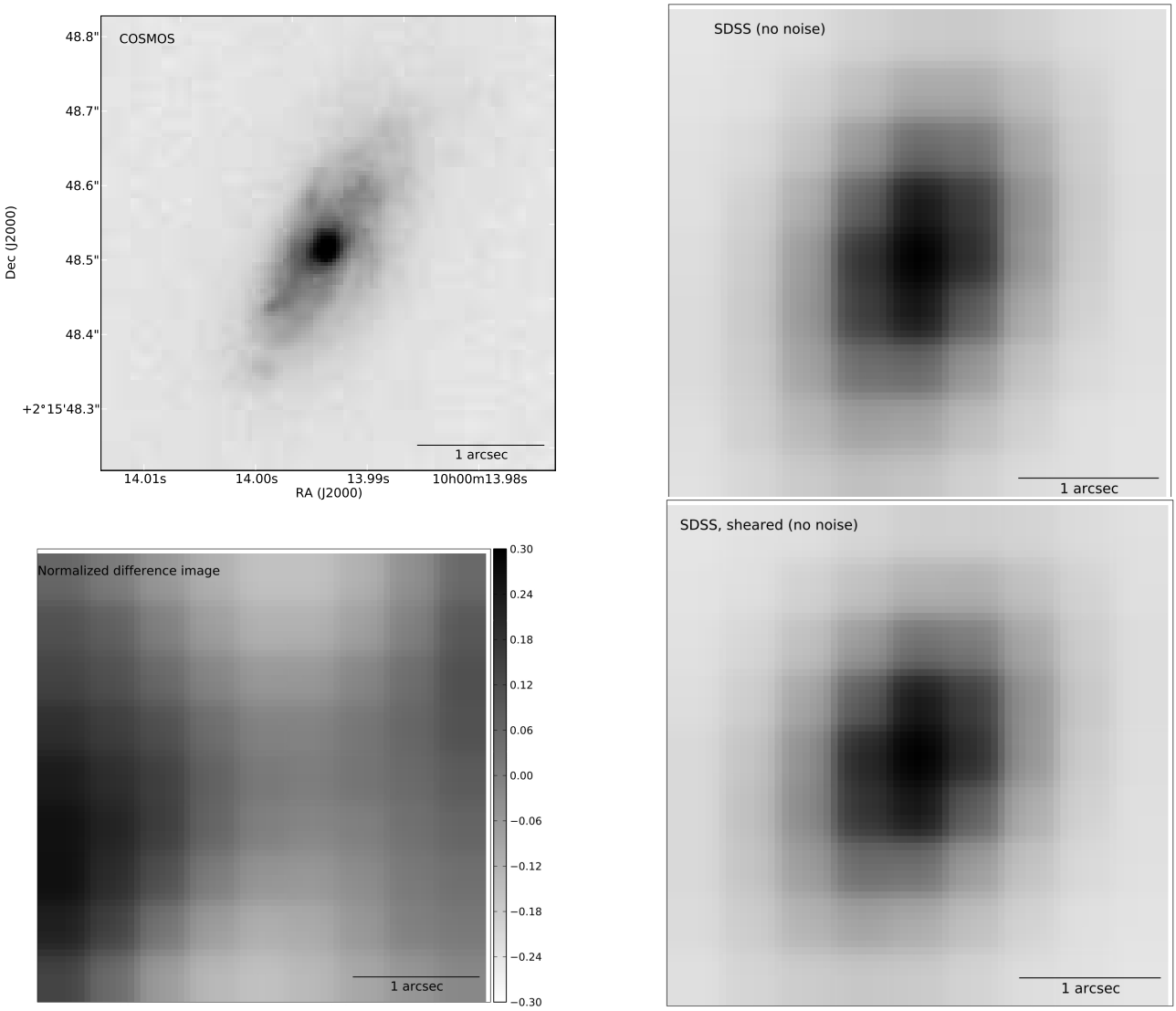

Figure 4. Example of how the SHERA processing changes the galaxy images. *Top left:* The original galaxy image in COSMOS, on a linear scale. *Top right:* The appearance of the galaxy in SDSS after PSF-matching, before adding levels of sky noise consistent with SDSS. *Bottom right:* Same as bottom left, but with a significant shear in the horizontal direction, $\gamma_1 = 0.1$. *Bottom left:* Difference image between the sheared and unsheared simulated image, normalized by the unsheared image. Because the differences are at most a few tens of per cent, they are difficult to pick out visually by comparing the top and bottom right images.

to study the distribution of $\Delta\gamma_1/\gamma_1$ and $\Delta\gamma_2$. We find that this distribution is mildly non-Gaussian (with positive kurtosis), and has a median value of $\Delta\gamma_1/\gamma_1 = 1.6 \times 10^{-5}$ and $\Delta\gamma_2 = 1.5\times10^{-6}$. This result suggests that on average, when simulating a sample of $\gtrsim 1000$ galaxies, the simulated shears are equal to the requested ones to extremely high accuracy. Moreover, the act of shearing one component does not lead to any significant spurious shear in the other component.

However, we should also consider the width of the distributions of $\Delta\gamma_1/\gamma_1$ and $\Delta\gamma_2$. If the distribution is broad, then when simulating a few individual galaxies, there could be some systematic deviation from the desired shear value which does not average out as it would when simulating many galaxies. The ensemble 68 per cent confidence intervals are $-0.0015 < \Delta\gamma_1/\gamma_1 < 0.0032$ (the median is not at the centre of this range because it is a skewed distribution) and $|\Delta\gamma_2| < 3.5\times10^{-4}$ (this distribution is not skewed, presumably because no shear was actually applied). We therefore conclude that for any individual simulated galaxy, (a) when applying a shear, there is a 68 per cent chance that the actual applied shear will be within $[-0.15, 0.32]$ per cent of the desired shear, and (b) shear components to which we do not intentionally apply a shear remain unsheared at the level of a few $\times10^{-4}$. Thus, the interpolation is sufficiently accurate to precisely shear the galaxies on average (that is, that there is no systematic problem with the applied shears) and even for single galaxies, the applied shears are correct at the level of a few tenths of a per cent.

The other operation for which we must use interpolation is the image resampling. There may be a concern that the tests described above are not an adequate test of the interpolation for resampling, for the following reason: when we apply a (typically small) shear, the pixel grid is not highly distorted near the centre of the galaxy. This means that the

interpolation is being used to estimate values very close to being on the pixel grid, which should not be too difficult. However, when we resample to some arbitrary pixel grid, we might end up interpolating (even near the image centre) to some locations that are not close to lying on the pixel grid. We therefore require a test of the interpolation that samples the image in a more general way than the above test.

Here we present a test of the images after pseudo-deconvolution, shearing, PSF-matching, and returning to real space - in other words, the actual point in SHERA where resampling takes place. The test is that instead of resampling the images, we apply a random rotation, and compare the change in the moments with the expected change. We know exactly how the galaxy ellipticities should transform:

$$\begin{aligned} e_{1,\rm rot} &= [\cos(2\theta_{\rm rand})]e_1 + [\sin(2\theta_{\rm rand})]e_2 \\ e_{2,\rm rot} &= -[\sin(2\theta_{\rm rand})]e_1 + [\cos(2\theta_{\rm rand})]e_2. \end{aligned} \quad (37)$$

An additional test is to ensure that the area implied by the adaptive moments ($(M_{xx}M_{yy} - M_{xy}^2)^{1/2}$) is unchanged by rotation.

When we carry out this test, we find that there is a non-zero but extremely small systematic change in the ellipticities (compared to the expected ellipticities after rotation): typically -1.3 and $+2.6 \times 10^{-6}$ for e_1 and e_2, respectively. We also find a tiny but statistically significant change in the areas implied by the adaptive moments, at the level of -8×10^{-7}. These numbers are sufficiently small that they are truly subdominant to other systematics issues that arise in any realistic lensing analysis.

8.2 Simulated galaxies compared to real data

Another important test for SHERA is to compare the simulated SDSS images of COSMOS galaxies with the real SDSS images of those galaxies. Here, we will describe several tests.

8.2.1 Galaxy numbers

As described previously, the sample of galaxies for which we have generated COSMOS postage stamps contains 26 113 galaxies (Sec. 4.1). This number was reduced to 25 527 (Sec. 6.2) when we require that the postage stamps go successfully through our postprocessing (to mask out additional objects, etc.) and then to 17 706 when we require that the galaxies lie in regions considered photometric in the SDSS imaging (Sec. A3).

There is one additional cut that we must impose after convolution to match the SDSS PSF. This cut relates to the fact that the original postage stamp sizes were estimated based on a circularly-averaged characteristic radius, which means that for very large and flattened galaxies, some flux might go off the edge of the convolved postage stamp in the direction of the galaxy major axis. To test for this issue, we processed all of the 'noiseless' simulated images, comparing the flux in (a) the pixel with the maximum flux, versus (b) the pixel with the maximum flux when considering only those pixels at the very edge of the postage stamp. We then eliminated those galaxies for which the latter was > 0.01 times the former. This left us with a final galaxy sample for all tests of 17 667 galaxies (some of them too faint to measure in the SDSS images).

8.2.2 Comparison with real data

The first comparison we make is between the simulated images (without shear or 90 degree rotation) and the actual SDSS images, for those that are detected. In principle, the images should be the same except for noise and the centroiding of each object within the central pixel (which we have made no attempt to match).

We begin by comparing the results for the noiseless simulations against those with the original SDSS data. In this case, there are 9469 galaxies that have measurable galaxy shapes (with re-Gaussianization) both in the real data and in the simulations; of those, 6361 pass our resolution cuts in both cases. We restrict the comparison of shapes to that sample of 6361, which should be fairly similar to the source catalogue except without a cut on magnitude, which would remove another ~ 30 per cent of the galaxies. The results are shown in Fig. 5, which shows that for both the observed ellipticities (e_1, e_2), and for the PSF-corrected $(e_{1,\rm corr}, e_{2,\rm corr})$, the median trend is for the simulated values to be equal to the ones in the real data (modulo noise, which tends to cause scatter in the vertical direction, since it is present in the real data but not in these simulations). This finding suggests that the simulation pipeline is indeed providing realistic data.

The apparent exception to the close comparison between simulated and real data is the R_2 comparison, which shows a distinct trend towards better resolution in the real data than in the simulations. There are two causes for this finding: the first is that we are imposing the R_2 cuts in different ways in the simulated and real data, since the former lacks noise. This results in a form of Malmquist bias, given that we impose the R_2 cut on the 'true' resolution in the simulation but on the noisy R_2 in the real data, which means that at the low resolution end of the sample, there is an induced bias when comparing the noisy versus the noiseless results. Indeed, this bias essentially vanishes if we make the same plot using the R_2 for the simulations with added noise.

However, even ignoring the very low resolution end, we can see that there is a weak (few per cent) tendency for galaxies to be scattered preferentially towards the upper left part of the plot. Detailed examination of some galaxies in that part of the figure suggests that while some are noise fluctuations in the real data, others are due to deblending failure. There are multiple nearby objects in reality, which are resolved in COSMOS, so that the additional objects besides the central galaxy were masked in our processing of the postage stamps; but the blend was not resolved in SDSS and hence was treated as one larger object. A careful study of these simulations can therefore be used to study deblending failures in ground-based data.

8.2.3 Comparison between original and rotated

As an additional sanity check, we also show a comparison between the shapes for the original and the rotated images, in the case of no added shear, but with added noise. For the sake of simplicity, we show only one shear component; results for the other are comparable. Here, we rely on the fact that

- the intrinsic shapes should be the opposite of each other, i.e. $e_{\rm orig,int} = -e_{\rm rot,int}$; and

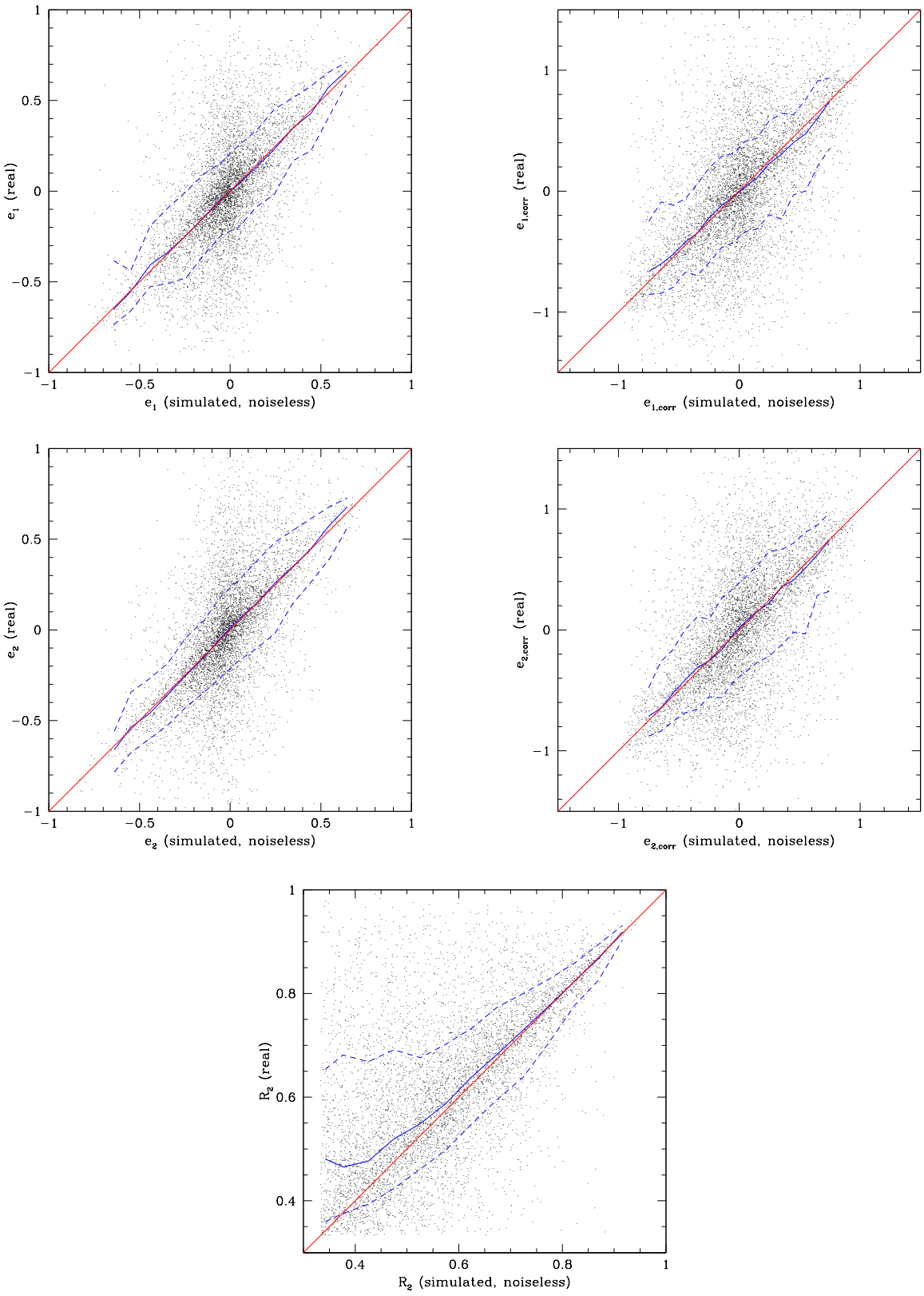

Figure 5. Basic shape comparison for real SDSS data versus (noiseless) simulated data, with points for each simulated galaxy and trend lines indicating the median (solid) and 68 per cent CL (dashed). For comparison, the 1:1 line is shown in all cases. *Top left:* Observed e_1 shape component (along the pixel direction) of the PSF-convolved galaxy image in the simulation without added noise versus in the real data. *Top right:* Same as left, but after PSF correction. *Middle row:* Same as top row, but for the e_2 ellipticity component. *Bottom row:* Galaxy resolution compared to the PSF in the simulation versus in the real data.

- any systematic additive component to the shapes from the PSF should be the same, i.e. $e_{\rm orig,sys} \approx e_{\rm rot,sys}$.

As a rule these additive systematic components will not cancel out over all the galaxies, because of the tendency for there to be a coherent PSF ellipticity in any given field that results in the systematic components of the galaxy ellipticities having the same sign.

Thus, when we plot $e_{\rm orig}$ versus $-e_{\rm rot}$, we should find that before PSF correction, the results are offset from the one-to-one line (but are parallel to it), and the results are returned to the one-to-one line after PSF correction. These results are shown in Fig. 6, and are entirely consistent with our expectations.

8.3 The need for pseudo-deconvolution

Before using our simulations to test the impact of pseudo-deconvolution (removal of the ACS PSF), we first consider the basic reasons why it may be important to include in a simulation pipeline that is meant to be able to accurately simulate ground-based data with a wide range of observing conditions.

Though we have focused on the ACS in this paper, the importance of pseudo-deconvolution is likely generic to all space telescope data (including other *HST* cameras) since it is a feature of diffraction patterns. While the core of the PSF has a radius of $\sim \theta_{\rm D} = \lambda/D = 0.07''$ for ACS/$F814W$ (where λ is the wavelength of observation and D is the outer diameter of the telescope), the diffraction rings contain a significant amount of power. For example, an Airy disc scatters a fraction $\sim 2\pi^{-2}\theta_{\rm D}/\theta$ of the light to radii $> \theta$ (for $\theta/\theta_{\rm D} \gg 1$). Thus for a galaxy with scale radius $\gg \theta_{\rm D}$, the effect of the PSF on observed galaxy properties scales in proportion to $\theta_{\rm D}$ rather than $\theta_{\rm D}^2$ as one would expect based on Gaussian approximations or second moments. An equivalent effect can be seen in Fourier space: $\tilde{G}(\boldsymbol{k})$ for an Airy disc has the leading behavior $1 - 2\pi^{-2}\theta_{\rm D}|k| + \ldots$ rather than having the first nontrivial term be k^2. Thus diffraction even by a large aperture (small $\theta_{\rm D}$) has an effect even for long-wavelength features in the image.

We can see one manifestation of this effect in Fig. 2, which shows the azimuthally-averaged Fourier space representation of the ACS PSF. While the ACS PSF is always above the SDSS PSF in that plot, indicating that the ACS PSF preserves more information than the SDSS PSF at all values of wavenumber k, it is nonetheless the case that it is tens of per cent below 1 at the band limit of the SDSS PSF, primarily because of the large-scale impact of the diffraction rings.

The above argument provides the justification for including pseudo-deconvolution as part of SHERA, given our intention that it should be useful for simulating ground-based imaging data under a wide range of observing conditions. However, it is not immediately obvious, for the case of data with typical seeing of $\sim 1.2''$ such as SDSS, that the pseudo-deconvolution is necessary for accurate image simulations. Here, we address this question using simulations for which the pseudo-deconvolution was not performed. That is, instead of removing the ACS PSF on scales that we will want to use from the ground, shearing, and then finding a matching kernel to the ground-based PSF, we simply shear

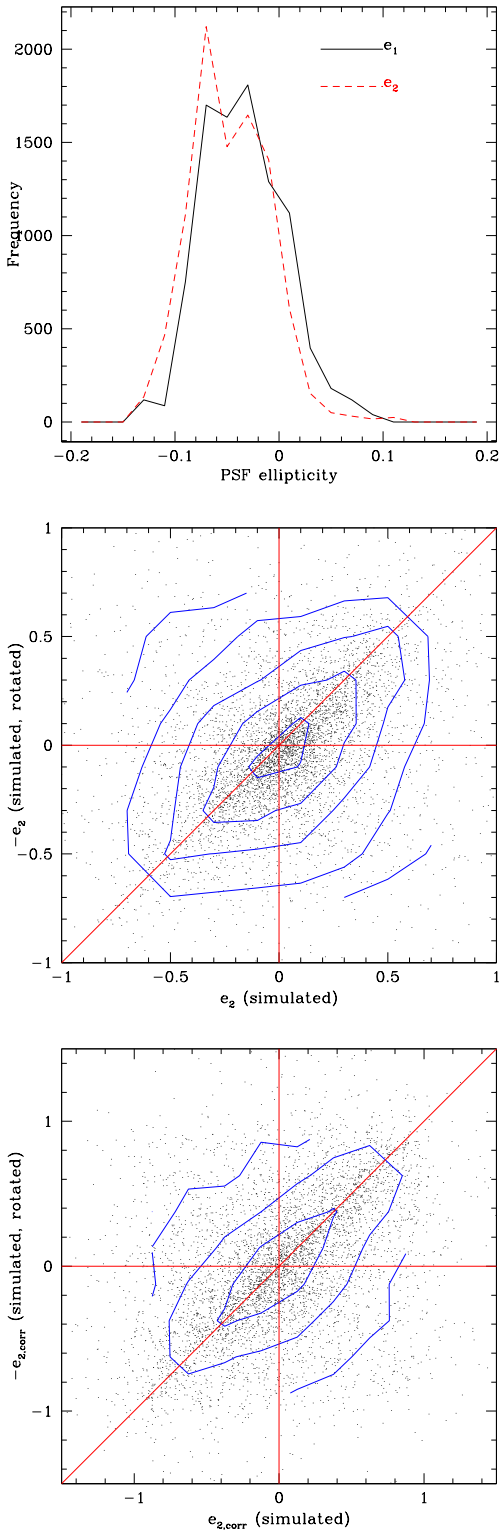

Figure 6. Shape comparisons for the galaxy images in their original orientation, and with a 90 degree rotation (using the same, non-rotated PSF). *Top:* Histogram of PSF ellipticities in the COSMOS field, which shows a coherent tendency towards $e_1 < 0$ and $e_2 < 0$. *Middle:* Observed e_2 shape of the PSF-convolved galaxy image in the original and rotated simulation images. *Bottom:* Same as middle, but after correction for the effects of the PSF.

and then convolve the data directly with the SDSS PSF, ignoring the ACS PSF entirely. This procedure was used for the STEP2 simulations (Massey et al. 2007a).

The results of comparing these simulations without pseudo-deconvolution, to the regular SHERA simulations without added noise, are shown in Fig. 7. Statistical analysis reveals the same trends in the data with noise, however they are less visually apparent.

As shown in the top panel of Fig. 7, when we compare individual galaxy ellipticities in the SHERA simulations and those simulations without pseudo-deconvolution, the latter tend to be rounder. The effect is, unsurprisingly, worse at large ellipticity. In the middle panel, we can see that the observed sizes are also affected: the galaxies appear to be larger compared to the SDSS PSF than they do in the simulations that account for the ACS PSF. As expected, the trend is more important for less well-resolved galaxies. Finally, we can see on the bottom that there is a concrete effect on the histogram of total ellipticities, with the trend suggested in the top panel that the simulations without pseudo-deconvolution yield a rounder galaxy population overall.

As a consequence of the overall rounder galaxy population, the inferred galaxy RMS ellipticity $e_{\rm rms}$ is ~ 0.31, in contrast to the finding from simulations including pseudo-deconvolution (Fig. 10) that it is ~ 0.36. Moreover, we find that the inferred shear changes slightly, becoming less negative by 1 per cent. Given the evidence that the PSF-matching is important in determining the observed galaxy properties at the $\sim$ 5–10 per cent level, and Sec. 9.2 showed that the shear calibration for re-Gaussianization depends on galaxy properties, the different derived shear calibration is likely due to the fact that not deconvolving the ACS PSF is equivalent to simulating a slightly larger, rounder galaxy population. This fact does *not* invalidate the utility of the STEP2 simulations for basic testing of PSF-correction algorithms; it simply means that to constrain shear calibrations in some hypothetical ground-based dataset to better than 1 per cent for this particular galaxy population, one should use simulations that (a) more closely mimic the imaging conditions at that particular telescope, (b) include other steps in the image processing, such as the need to combine multiple exposures, and (c) include pseudo-deconvolution to more faithfully represent the intrinsic properties of the galaxy sample.

The effects that are described in this section will be more important for several limiting cases: (1) ground-based images with better resolving power than SDSS, such as Subaru Suprime-Cam (for which the median seeing is $0.7''$ and the pixel size $0.2''$, both numbers a factor of ~ 2 smaller than for SDSS) and (2) ground-based images that are deeper, including more galaxies that are intrinsically small and faint. We have explicitly tested the first scenario, using a typical Subaru Suprime-Cam PSF, and found that the effects of ignoring pseudo-deconvolution on the observed galaxy sizes are nearly twice as large as for SDSS. Thus, for all upcoming surveys, image simulations that rely on space-based data to precisely calibrate shears must account for the PSF if they want to simulate a realistic galaxy population using SHERA.

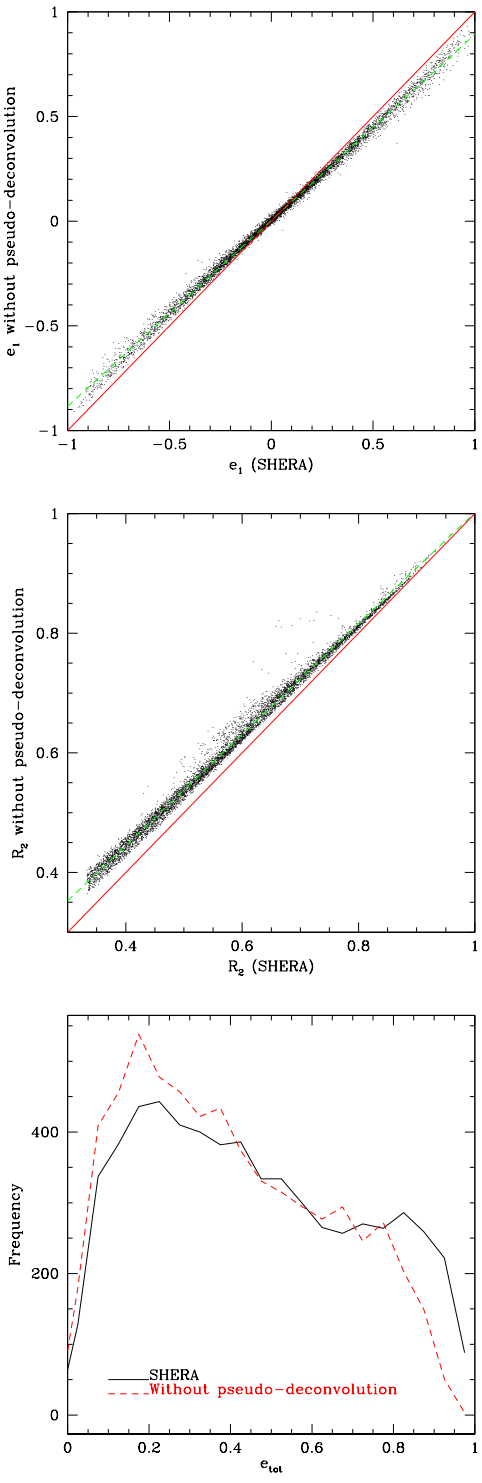

Figure 7. Comparison of SHERA simulations versus those that do not include the pseudo-deconvolution of the ACS PSF. *Top:* Scatter plot comparing the values of one ellipticity component, e_1, for each galaxy. The solid line shows the 1 : 1 line; the dashed line shows the best-fit line, reflecting a factor of 0.9 multiplicative offset. *Middle:* Scatter plot comparing the values of resolution factor, R_2, for each galaxy. The dashed best-fit line reflects a $\sim$ 15 per cent offset for the poorly-resolved galaxies. *Bottom:* Histogram of $e_{\rm tot} = (e_1^2 + e_2^2)^{1/2}$ values in the two simulation sets.

8.4 Impact of using Tiny Tim rather than observed PSFs

As pointed out in Sec. 6.3, there are some known issues with the Tiny Tim PSFs that are used for PSF correction in Leauthaud et al. (2007) and Massey et al. (2007a), and that are used in this work and included with the associated data release. Consequently, we must estimate the impact of using them rather than real stars (from dense stellar fields, with the same primary/secondary separation) when performing the pseudo-deconvolution step before matching to the target ground-based PSF.

For this test, we used a random subsample of COSMOS galaxies, and compared the observed resolution factors (R_2) with respect to the SDSS PSF when we used SHERA with the same input parameters, only varying which COSMOS PSF was used for the pseudo-deconvolution. We found that for well-resolved galaxies, the R_2 value was 0.4 per cent larger when using the real PSF stars than using the Tiny Tim models; at our lower resolution limit, they were typically 1.2 per cent larger. For context, we saw in Fig. 7 that at the resolution limit, if we did not pseudo-deconvolve but instead ignored the ACS PSF entirely, the resolution factors in the simulated data differed by 16 per cent. Thus, crudely speaking, pseudo-deconvolution using the Tiny Tim PSF models effectively removes $\gtrsim 93$ per cent of the impact of the ACS PSF in the final simulated images.

The practical barrier at this time to simply using the stellar images for pseudo-deconvolution is that the stellar fields are typically not deep enough to get a very high S/N PSF estimate on a per-star basis; the first diffraction ring is barely, if at all, visible when looking at a single star. Thus, a reliable PSF interpolation routine would be necessary to fit for a high S/N PSF model as a function of CCD position, which includes a non-negligible amount of development and testing to validate it. While such development is ultimately necessary for very high precision tests using SHERA, we defer it to future work.

8.5 Impact of noise in original COSMOS images

The noise in the original COSMOS galaxy postage stamps is sheared and convolved with the target PSF. In this section, we concretely demonstrate the impact of that low noise level on the simulated images.

To carry out this test, we take a subset of the simulated SDSS images, and do the following operations:

- We start with the CTI-corrected and cleaned galaxy postage stamps from Sec. 6, but in addition to masking out all additional objects in the postage stamp, we also mask out the central object. This gives us a standard galaxy-size postage stamp but with only a correlated noise field, no real objects.
- We process it with a modified version of SHERA using the same target PSF as when simulating the real SDSS data, including forcing the code to use the same normalizing factors for the flux as when making the simulations that do have the galaxy present. This ensures that the normalization of the resulting sheared, PSF-convolved noise field is the same as that in the standard galaxy simulations. To make it easier to detect systematic effects, we impose a relatively large shear, $\gamma_{\rm input} = 0.1$.
- We then add the resulting sheared, correlated noise fields to the (shear-free) galaxy simulations used in Sec. 8.2, without and with noise added to match SDSS.

We compare the original noiseless simulations versus those that have the new correlated noise fields added, constructing $\Delta\hat{e}_1$, and $\Delta\hat{e}_2$ (for the PSF-corrected galaxy shapes). This comparison reveals systematic offsets in properties due to the correlated noise fields that result from running a COSMOS noise field through SHERA. The results, with different input shear values ($\gamma_{\rm input}$) for the noise fields, are consistent with

$$\frac{\Delta\hat{\gamma}}{\gamma_{\rm input}} \sim 0.01. \quad (38)$$

As a practical consequence, this means that the original noise in the COSMOS images, when sheared, does not affect our ability to test shear recovery to the per cent level. However, if we wish to constrain shear calibration to well below the per cent level, then this effect (in addition to the effects in Sec. 8.4) must be accounted for. We defer consideration of this issue to future work.

9 RESULTS: SHEAR CALIBRATION

In this section, we present one example usage of the SHERA pipeline to assess the calibration of lensing shear measurements using the re-Gaussianization PSF correction method.

For these tests, we chose 14 sets of (γ_1, γ_2) shears to simulate; these are shown in the top panel of Fig. 8. For each of the 17 706 galaxies used for the simulations to validate the pipeline (Sec. 8.2), we used SHERA to generate 56 additional simulated galaxies: 14 shear sets, 2 noise options (noiseless and noisy), and 2 orientations (original and 90 degree rotated). We then select galaxies in various ways (to be described shortly), and defined a weight function for each galaxy:

$$w_i = \frac{w_{{\rm COSMOS},i}}{\sigma^2_{e,i} + e^2_{\rm rms}}. \quad (39)$$

Here the numerator $w_{{\rm COSMOS},i}$ is the inverse of the postage stamp selection function (Sec. 4.1 and Fig. 1) meant to remove our selection bias against physically large galaxies. The denominator only is significant for shear estimates using the simulations with sky noise, since the shape measurement error is negligible for those without added noise. For typical galaxy-galaxy lensing analyses, there is an additional factor in this weight function: Σ_c^{-2}, which corresponds to optimal weighting in the case that lens and source redshifts are both known. For the simulations, we cannot easily include such a factor, because simulating the SDSS photo-z would require simulating *ugriz* data and processing it with the SDSS PHOTO pipeline.

To estimate the shear, we then defined

$$\hat{\gamma}_\alpha = \frac{\sum_i w_i(\gamma_{\alpha,i,{\rm orig}} + \gamma_{\alpha,i,{\rm rot}})}{4S_{\rm sh}\sum_i w_i} \quad (40)$$

in terms of the PSF-corrected shapes, for shear components $\alpha = 1, 2$ and galaxies i. The $S_{\rm sh}$ factor, or shear responsivity, represents the response of our particular ellipticity definition Eq. (9) to a shear; it is equal to $1 - e^2_{\rm rms}$.

9.1 Without sky noise

We first present results using the 'noiseless' simulations, which we expect to do with very small statistical errors since there is essentially no measurement error, and the use of original and rotated shapes should effectively eliminate the shape noise. In order to select an approximately reasonable galaxy population for this test, we use the COSMOS $F814W$ magnitudes and the typical SDSS colours to impose an approximation of the $r < 21.8$ cut (corresponding to that for the real source catalogue). We also require a resolution factor $R_2 > 1/3$ for both the original and rotated galaxy; this results in a sample of 6 160 galaxies. The comparison between the estimated shears $(\hat{\gamma}_1, \hat{\gamma}_2)$ and the true ones for each of the 14 simulations with shear is shown in Fig. 8.

As shown, there is a clear detection of non-zero calibration bias and additive PSF systematics. When fitting to

$$\hat{\gamma}_\alpha - \gamma_\alpha = m_\alpha \, \gamma_\alpha + c_\alpha \ , \tag{41}$$

both the slope (calibration bias) m and the additive constant c differ from zero. The calibration biases are -1.6 ± 0.1 and -2.7 ± 0.1 per cent for the two shear components. The fact that these biases differ for the two components, and that the latter is worse than the former, is consistent with results of High et al. (2007) and Massey et al. (2007a). The standard explanation is that the pixel resolution is effectively a factor of $\sqrt{2}$ worse along the diagonals of the pixels than along the pixel direction. If we remove the weighting in Eq. (39), then the calibration biases change by 0.1 per cent, the size of the 1σ error. The sign and magnitude of this change can be explained by the weak but non-negligible correlation between the galaxy weights $w_{\rm COSMOS}$ (to account for the inability to create postage stamps for some of the larger galaxies) and the galaxy size, given the trends we will see in the calibration bias with galaxy size in Sec. 9.2.

The nonzero additive contamination (c values) can be explained by the nonzero average PSF ellipticity, which is imperfectly removed from the galaxy images by re-Gaussianization. For context, the typical PSF ellipticity in SDSS is ~ 0.05, so the fractional contamination is $|c_1/e_{1,\rm PSF}| \sim 5 \times 10^{-3}$.

9.2 Dependence on sample properties (noiseless)

In figure 5 of Mandelbaum et al. (2005), predictions were shown for the shear calibration bias for the re-Gaussianization method using noiseless simulations, for exponential and de Vaucouleurs galaxies, using a Kolmogorov turbulence-induced profile, i.e. $\ln \tilde{G}(\boldsymbol{k}) \propto -k^{5/3}$. As shown there, the calibration biases depend on the galaxy profile, being more negative for de Vaucouleurs profiles than for exponentials; on the resolution factor, being more negative at intermediate resolutions ($R_2 \sim 0.6$) and closer to zero for resolutions at the lower (1/3) and upper (1) limits; and on the intrinsic ellipticity, being more negative for more intrinsically circular galaxies. We now test all of these predictions, again in the case without measurement noise.

To carry out these tests, rather than computing an ensemble $\hat{\gamma}$ to compare with the input value via weighted summation over all the individual shear values, as in Eq. (40), we instead consider individual shear estimates for every single galaxy. To estimate a shear for each galaxy, we use the orig-

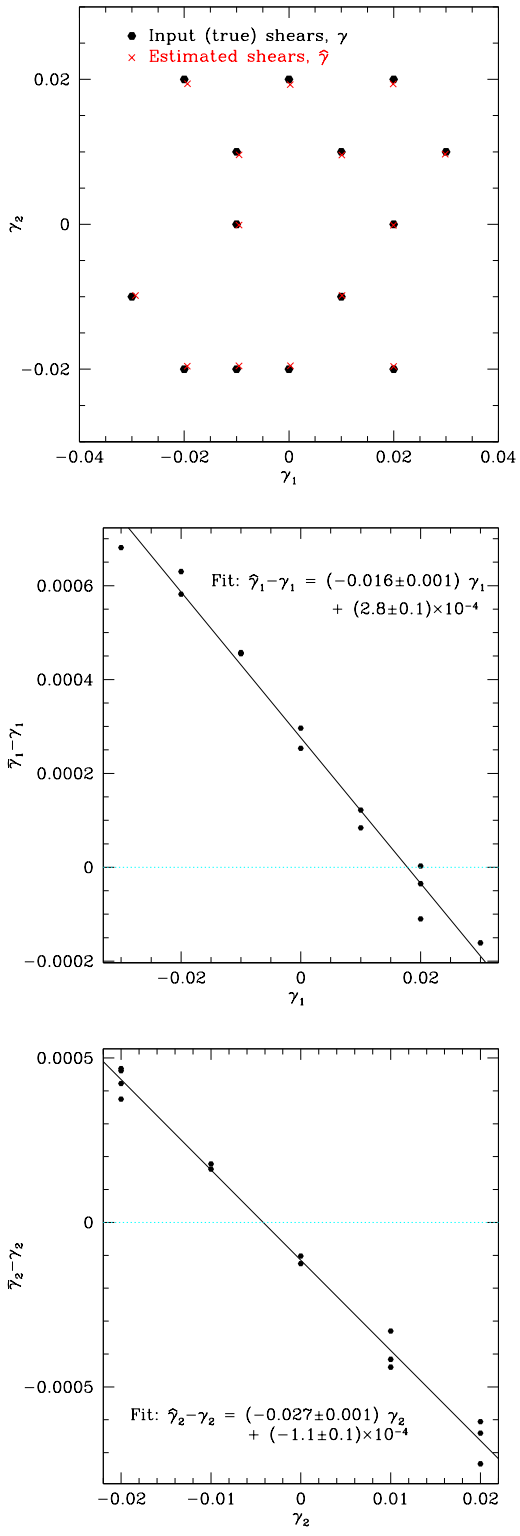

Figure 8. Results of shear calibration tests for the re-Gaussianization PSF-correction technique, using the 'noiseless' COSMOS simulations with flux and resolution cuts. *Top:* The true input shear values, and the estimated ones. *Middle:* The error in recovered shear component 1, $\hat{\gamma}_1 - \gamma_1$, as a function of the input shear. The best-fitting line is also plotted. *Bottom:* Same as middle, but for the other shear component.

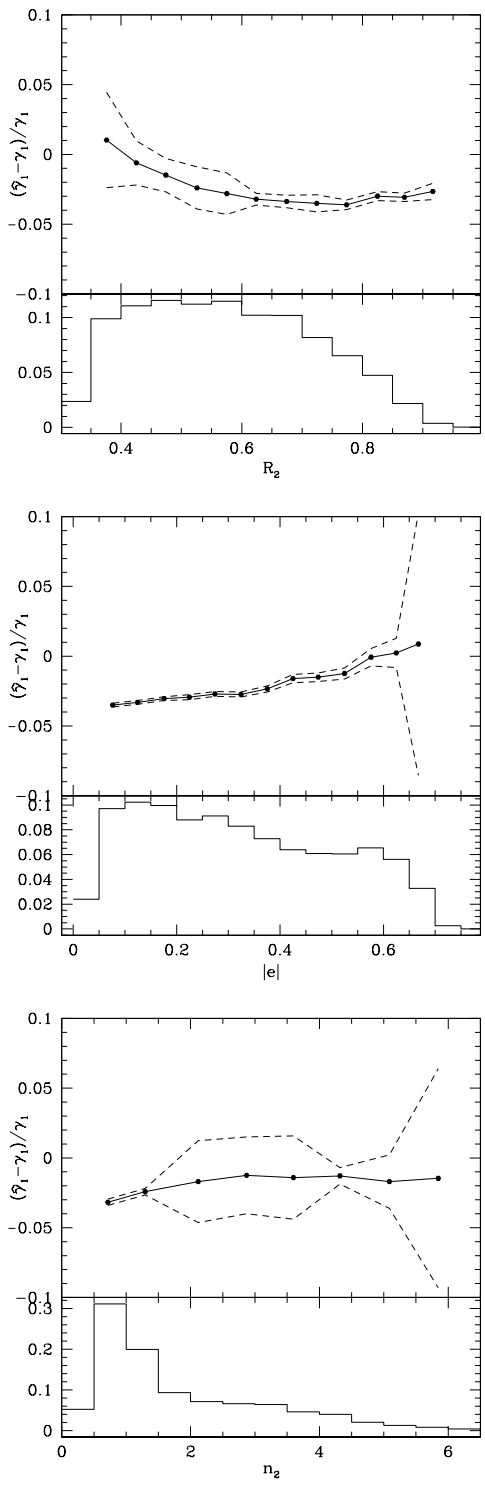

Figure 9. Results of shear calibration tests for the re-Gaussianization PSF-correction technique, using the 'noiseless' COSMOS simulations with flux and resolution cuts. *Top:* The fractional error in the recovered shear as a function of the galaxy resolution with respect to the PSF, R_2, along with the histogram of R_2 values for the noiseless simulations. The points and solid line show the median trend; the dashed lines show the statistical uncertainty in the trend-line. *Middle:* Same as top, but as a function of total ellipticity $|e|$. *Bottom:* Same as top, but as a function of Sérsic n_s as determined from the COSMOS images.

inal and rotated shape measurements for each component (4 measurements), and write four equations based on eq. (2-13) of Bernstein & Jarvis (2002) to express those observables in terms of the intrinsic shape and the applied shear (4 unknowns). These equations are nonlinear functions of the intrinsic shape and applied shear; we solve this nonlinear system of equations using the IDL implementation of Broyden's method to estimate $\hat{\gamma}_{\alpha,i}$ (for shear component α, galaxy i).

Given the individual shear estimates, we can compute the fractional error in each one, $(\hat{\gamma}_{\alpha,i} - \gamma_\alpha)/\gamma_\alpha$ in bins in galaxy properties. The properties used for this test are the resolution factor R_2; the total ellipticity $e_{\rm tot} = \sqrt{e_1^2 + e_2^2}$; and the Sérsic n_s derived from single component fits to the COSMOS images from Sargent et al. (2007), using GIM2D (Marleau & Simard 1998). The results are shown in Fig. 9.

As shown in the top panel, we find a calibration bias that approaches zero for the lowest and highest resolutions in our sample, and goes as low as -4 per cent for the galaxies at $R_2 \sim 0.7$. This finding is qualitatively similar to that from the noiseless simulations of Mandelbaum et al. (2005), with the difference being that these results intrinsically average over a more realistic galaxy population (all morphologies rather than single-component Sérsic profiles with $n_s = 1$ and 4) and real PSFs.

The middle panel of Fig. 9 shows that the calibration bias tends to be most negative (~ -3 per cent) for galaxies that are nearly circular, and increases to 0 for $|e| \sim 0.6$, becoming slightly positive at even higher ellipticities (where, however, there are very few galaxies and therefore the statistical significance of the trend above $|e| > 0.6$ is unclear). This trend is again similar to that from Mandelbaum et al. (2005).

The bottom panel of Fig. 9 shows the trend with Sérsic n_s, which gives a calibration bias that is most negative for low n_s (exponential galaxies) and is closer to zero for higher n_s. This finding is the opposite of that from Mandelbaum et al. (2005); however, it is important to note that in this case the n_s values are not exact representations of the real galaxy morphologies, given that most galaxies show some deviation from a perfect elliptical Sérsic profile (either having more small-scale structure, or being clearly composed of multiple components such as a bulge and a disk). Thus, it is unclear that the results shown here as a function of n_s can truly be directly compared with those from Mandelbaum et al. (2005), without first assessing which of the COSMOS galaxies are in fact consistent with a featureless Sérsic model. Moreover, the statistical significance of the observed trend is fairly weak.

9.3 Noisy simulations

We now consider the shear calibration bias in simulations with sky noise. However, because the sky level in the SDSS imaging of the COSMOS field is atypically high (Sec. A1), we use a set of simulations that are otherwise identical to the ones from Sec. 9.1, but with sky noise that is 15 per cent lower (in the standard deviation). The more typical noise level in these simulations makes them more like typical SDSS data.

There is an important subtlety when using a sample that has noise to estimate shear calibration bias: we must

be very careful when selecting galaxies to use for the shear estimation. In Sec. 9.1, we simply approximated an $r < 21.8$ cut in order to get a roughly similar galaxy population as in the real data. Here, however, we know that galaxies that have a noise fluctuation such that they are harder to detect would realistically not be included in our sample, and that is a good thing given that their shears should be unreasonably difficult to measure. In order to perfectly mimic our sample selection in the real data, we would have to process the simulated images in the exact same way as the real data, using PHOTO. However, there are other practical obstacles to constraining the shear calibration in all of SDSS using this simulation set (e.g., the fact that we have not sought to carefully mimic the distribution of observing conditions throughout the entire SDSS area). So, we instead use a simpler approximation of our selection in the real data, as a basic demonstration of the power of the SHERA code rather than as a quantitative estimate of the SDSS shear calibration bias.

Our crude selection relies on the estimated shear measurement errors σ_γ for each galaxy. The re-Gaussianization code estimates σ_γ (per component) by taking the input value of sky variance $\sigma^2_{\rm sky}$ from Eq. (A2), and using (Bernstein & Jarvis 2002)

$$\sigma_\gamma = \frac{\sigma_e}{2} = \frac{\sqrt{4\pi n}\sigma_{\rm sky}}{f_w} = \frac{2}{S/N} \, , \qquad (42)$$

where f_w is the weighted flux (by the adaptive moment matrix). This equation is only approximate, and assumes Gaussianity of the PSF-convolved galaxy image.

Thus, our approach to object selection in these simulations is as follows:

(i) We examine the real SDSS source catalogue to find what S/N is implied by the σ_γ values at our limiting magnitude $r = 21.8$. While there is a range of σ_γ values at fixed magnitude, we find that $r < 21.8$ corresponds to $\sigma_\gamma \lesssim 0.21$ (or $S/N > 9.5$).

(ii) We impose that σ_γ cut on the original and rotated simulated images[20]. In practice, for a given set of noisy simulations, typically 4100 galaxies pass this cut, the resolution cut, and the $e_{\rm tot} < 2$ cut.

The first aspect of the shear estimation that we can test using the noisy simulations is the shear responsivity calculation, which is in the denominator of our shear estimator Eq. (40) and is

$$S_{\rm sh} = 1 - e^2_{\rm rms} \, , \qquad (43)$$

where the rms ellipticity per component is ideally defined as a weighted sum over the ellipticities of the source population,

$$e^2_{\rm rms} = \frac{1}{2}\left[\frac{\sum_i w_i (e_1^2 + e_2^2)}{\sum_i w_i}\right] \qquad (44)$$

given true, noiseless, e_1 and e_2 values (the mean ellipticity per component, $\langle e_1\rangle = \langle e_2\rangle = 0$). In real data, we lack a noiseless estimator of e_1 and e_2, so we must estimate $e_{\rm rms}$ using our noisy estimated $\hat{e}_1$ and $\hat{e}_2$:

$$\hat{e}^2_{\rm rms} = \frac{1}{2}\left[\frac{\sum_i w_i (\hat{e}_1^2 + \hat{e}_2^2 - 2\sigma_e^2)}{\sum_i w_i}\right] . \qquad (45)$$

Errors in the estimated $e_{\rm rms}$ from Eq. (45) propagate into the shear estimates via Eq. (40).

For our noiseless simulations, we come as close as possible to being able to carry out a 'true' $e_{\rm rms}$ estimate, Eq. (44). In practice, these simulations do include a low level of noise from the COSMOS simulations, but we at least know that this will tend to increase the estimated $e_{\rm rms}$; thus, the $e_{\rm rms}$ from the noiseless simulations serves as an upper limit on the true $e_{\rm rms}$. Hence, we first estimate $e_{\rm rms}$ as a function of magnitude for the noiseless and the noisy simulations, to estimate how much the inaccurate σ_e estimates might be biasing $e_{\rm rms}$, $S_{\rm sh}$, and the estimated shears. The results of this estimate are shown in Fig. 10.

As shown, the RMS ellipticity is close to flat with magnitude in the noiseless simulations.[21] In contrast, in the noisy simulations, it appears to increase significantly at fainter magnitudes, even after our attempts to subtract off the measurement error. This result implies that our shape measurement errors are underestimated. Fig. 10 gives us a way to assess how much the estimated shear responsivities are incorrect due to our underestimated shape measurement error.

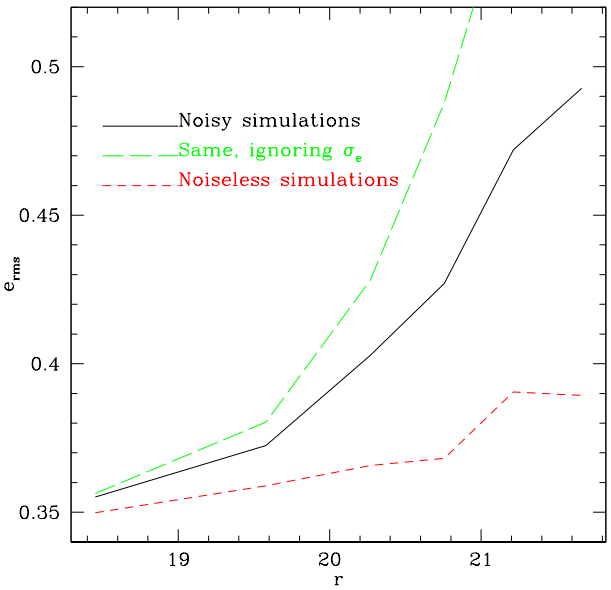

Figure 10. The RMS ellipticity $e_{\rm rms}$ as a function of the apparent magnitude. Results are shown for the simulated data with noise, before (long-dashed) and after (solid) subtracting off our estimates of the shape measurement error due to photometric noise. The results are also shown for the same galaxies using the ellipticities from the noiseless simulations (dashed line).

[20] Technically, in the real data, we impose our S/N cut in r. However, there is also a magnitude cut in i which, given the relation between the sky variances in the two bands and the typical galaxy colours, corresponds to a similar S/N cut in that band. Thus, requiring the magnitude and resolution cuts in r and i in the real data is parallel to our imposition of S/N and resolution cuts in the simulations for both the original and the rotated images.

[21] In an upcoming paper, Reyes et al. (2011, *in prep.*), we will present evidence that the deviations from flatness in these simulations are due to small levels of nonlinearity in the PSF correction that lead to non-Gaussian error distributions.

We find that for the noisy simulations, the responsivity is estimated as 0.84, whereas in the noiseless ones, it is 0.86. Thus, our responsivity is 2.5 per cent too low, so the shears are overestimated by this amount in the noisy simulations. In the text that follows, when we quote shear calibration biases for noisy simulations, they include this shear overestimation due to shear responsivity error.

The value of $e_{\rm rms} \sim 0.36$ in Fig. 10 may seem inconsistent with that from the COSMOS data for bright galaxies, figure 17 of Leauthaud et al. (2007), which gives $e_{\rm rms} \sim 0.27$. However, as described in Sec. 4.3, the shape estimates in these two works differ in use of circularly weighted (Leauthaud et al. 2007) vs. elliptical-weighted adaptive moments (this work), such that we *should* find a larger $e_{\rm rms}$ in this work. While Eq. (13) relating the two ellipticity measurements is only exactly valid in certain unrealistic limits (Gaussian profiles), we can nonetheless use it to estimate the effect of this different shape definition. If our simulation ellipticities are transformed using Eq. (13) to those that are expected using RRG, then the resulting $e_{\rm rms} = 0.28$, quite similar to that from Leauthaud et al. (2007). Residual difference may be due to the cases where Eq. (13) fails to relate the two ellipticities correctly.

Next, we carry out a similar shear calibration bias calculation as in Sec. 9.1, but with the noisy simulations, using the σ_γ cut discussed earlier in this section to remove those galaxies that have low significance detections. We use two independent noise realizations of each galaxy pair to reduce the noise. In comparison with the noiseless case shown in Fig. 8, for which we had found ensemble calibration biases of $m_1 = -1.6 \pm 0.1$ and $m_2 = -2.7 \pm 0.1$, the noisy case gives calibration biases of $m_1 = -3.8$ and $m_2 = -4.3 \pm 2.5$ per cent[22]. This result is just 2 per cent worse than the noiseless case; however, the net -4 per cent calibration bias also includes a $+2$ per cent bias due to incorrect shear responsivity, implying a -6 per cent bias due to insufficient dilution correction and noise rectification bias.

We can compare these results with noisy simulations against those from the STEP2 simulations (Massey et al. 2007a). There are a number of reasons why we do not expect the results to agree: for example, the fact that a deeper sample population was being simulated in STEP2, with intrinsically different properties; the fact that higher resolution Subaru PSFs and pixel scale were used in STEP2; and the fact that the ACS PSF was not pseudo-deconvolved before convolving with the ground-based PSF. Nonetheless, we compare against the following STEP2 results: the shear calibration bias for re-Gaussianization (denoted 'RM' in Massey et al. 2007a) was typically -2.5 per cent; and the shear calibration bias is more negative for fainter magnitudes. Our -4.0 ± 2.5 per cent calibration bias is statistically consistent with the STEP2 results. Moreover, the fact that the calibration bias became more negative as we moved from noiseless to noisy simulations is qualitatively consistent with the STEP2 result that calibration bias is more negative at fainter magnitudes (i.e., lower S/N). A detailed quantitative comparison is beyond the scope of this paper due to the many intrinsic differences between these simulations.

[22] When calculating unweighted sums over the galaxies, without the weight factor in Eq. (39), the calibration biases worsen by -2 per cent, just under 1σ. This difference reflects the fact that the bias is worse when we include galaxies near the flux limit, which get downweighted due to their larger σ_e.

9.4 Limitations of these results

The shear calibration bias estimates in this section were intended primarily as a demonstration of one possible application (out of many) of the SHERA pipeline. Here we summarize why the specific numbers presented here should not be used as a precise estimate of the shear systematics in science papers using the SDSS re-Gaussianization shape catalogue:

(i) In this section, we have averaged over all sources that are detected in the simulations. In practice, the source population that is used depends on the lens redshift, since photometric redshifts are used to (roughly) select those sources that are behind the lenses.

(ii) When calculating signals for the real data, there is an additional weight factor Σ_c^{-2} to achieve optimal weight in the estimate of $\Delta\Sigma$. This weight correlates with galaxy properties and, consequently, will change the mean calibration bias for a given sample population.

(iii) The range of observing conditions in the SDSS is quite broad. In practice these results might depend in detail on simulating a range of observing conditions.

(iv) The real data use r and i band averaged shapes. In practice these might have different shear calibration biases than the i band shapes used here, because of colour gradients changing the observed morphology slightly, and because of the different S/N of detection in the two bands.

(v) As demonstrated in Sec. 9.3, the estimate of shear calibration depends on how the sample is cut in S/N. Thus, our crude σ_γ cut must be replaced with a more realistic approximation of the sample selection used in the SDSS data, based on the model flux from PHOTO.

(vi) Using a realistic simulation, we should be able to understand the impact of selection biases in determining the shear calibration. Because the simulations described here have several atypical features (particularly the use of 90 degree rotated galaxy pairs), the selection biases do not operate in the same way here as in real data.

A precise calculation of the shear calibration bias for the real data would have to account for these effects.

10 DISCUSSION

We have described new, publicly-available software, SHERA, that can be used to simulate (optionally sheared) ground-based images with realistic morphologies and any PSF that has worse resolution compared to COSMOS. This software is independent of modeling assumptions about what galaxies or PSFs look like, properly handles the pixel response functions, and has been tested to sub-per cent precision (Sec. 8). The code has been publicly released, along with CTI-corrected, cleaned COSMOS galaxy postage stamps for a flux-limited sample at $F814W < 22.5$. This code should be highly useful for realistically assessing the systematics of lensing analysis (or indeed any other detailed image analysis, such as galaxy profile determination) in ground-based data, including the effects of a range of observing conditions. It

should also allow for assessment of parameter uncertainties and degeneracies, and selection biases, via the generation of many noise realizations for a single galaxy. As a basic demonstration, we have shown a crude estimation of shear calibration bias for SDSS single-epoch lensing analysis.

In order for the code and data that are described in this paper to be more broadly applicable, there are several improvements that would be needed. First, we would like the ability to simulate data in other passbands besides i (for which there is precedent, e.g. Ferry et al. 2008 used data from the Ultra Deep Field to do so). Realistic galaxies have colour gradients that will cause an intrinsically different appearance in significantly different bands. While this may be unimportant for current surveys that have statistical errors that are > 5 per cent, future surveys such as LSST that aim for better than 1 per cent precision in the lensing signal have correspondingly a need for very well-constrained shear systematics. Thus, such effects must be handled realistically, and it is possible that sufficient well-sampled data[23] in other bands and in random fields exists in the *HST* archive that could be used for this purpose. We specify random fields because those that were selected due to, e.g., presence of a galaxy cluster, may not have a representative morphological mix. There is additional value to obtaining data in other, random fields, given that even with the relatively large (for *HST*) size of the COSMOS field, it still exhibits significant cosmic variance (e.g., Kovač et al. 2010) in the redshift distribution, which may manifest at some level as an atypical morphology distribution.

Additionally, we need a way to simulate a deeper sample. Presently we have stopped at $I < 22.5$ because the method described here requires modification if the input images have non-negligible noise, and the COSMOS data have $S/N > 50$ for that magnitude range. Thus, we require either a generalization of the method to lower S/N in the input images, or we require deeper input data than is available in the COSMOS field. In some cases, the former would be possible: since the SHERA algorithm is a linear operation on the COSMOS postage stamps, one could propagate any noise covariance matrix through the pipeline and arrive at an output covariance matrix $N_{ij}^{\rm IN}$ on the output postage stamps. If the noise covariance in the data we wish to simulate is $N_{ij}^{\rm OUT}$, then so long as $\mathbf{N}^{\rm OUT} - \mathbf{N}^{\rm IN}$ is semi-positive definite, one could add in the appropriate additional noise and thereby extend the methodology of this paper to noisy input data. The software implementation of such a method, exploration of its range of applicability, and investigation of complications such as non-Gaussian noise is left to a future paper. In the opposite case, namely that where the input data has more noise in some mode than the data we wish to simulate, it seems likely that the problem is hopeless and deeper input data would be required.

Despite the need for future work to make the code and/or input dataset as useful as possible for lensing surveys that are coming up on the timescale of ~ 1 decade, we anticipate that SHERA v1.0 has numerous applications for better understanding of current data and those surveys that are starting in the next year, such as KIDS, HSC, and DES.

[23] Data with some instruments may not have a Nyquist-sampled PSF, depending on the choice of dither pattern.

ACKNOWLEDGMENTS

We thank the referee for many constructive comments about the organization and content of this paper. The authors would also like to thank Jim Gunn, Robert Lupton, Dustin Lang, David Hogg, Michael Blanton, Barney Rowe, Peter Capak, Chiaki Hikage, Uros Seljak, and Gary Bernstein for useful conversations about this project; and Eric Huff both for discussing it and giving the software a name. C.H. is supported by the US National Science Foundation (AST-0807337), the US Department of Energy (DE-FG03-02-ER40701), the Alfred P. Sloan Foundation, and the David and Lucile Packard Foundation. A.L. acknowledges support from the Chamberlain Fellowship at LBNL and from the Berkeley Center for Cosmological Physics. RJM is supported by STFC Advanced Fellowship #PP/E006450/1 and ERC grant MIRG-CT-208994. This work was done in part at JPL, run under a contract for NASA by Caltech.

The HST COSMOS Treasury program was supported through NASA grant HST-GO-09822. We wish to thank Tony Roman, Denise Taylor, and David Soderblom for their assistance in planning and scheduling of the extensive COSMOS observations. We gratefully acknowledge the contributions of the entire COSMOS collaboration consisting of more than 70 scientists. More information on the COSMOS survey is available at http://cosmos.astro.caltech.edu/. It is a pleasure to acknowledge the excellent services provided by the NASA IPAC/IRSA staff (Justin Howell, Anastasia Laity, Anastasia Alexov, Bruce Berriman and John Good) in providing online archive and server capabilities for the COSMOS data-sets.

REFERENCES

Abazajian K. et al., 2009, ApJS, 182, 543
Aihara H. et al., 2011, ApJS, 193, 29
Bartelmann M., Schneider P., 2001, Phys. Rep., 340, 291
Bernstein G., 2010, MNRAS, 406, 2793
Bernstein G., Jarvis M., 2002, AJ, 123, 583
Bertin E., Arnouts S., 1996, A&AS, 117, 393
Bridle S. et al., 2010, MNRAS, 405, 2044
Bridle S. et al., 2009, Ann. App. Stat., 3, 6
Dark Energy Survey Collaboration, 2005, preprint (arXiv:astro-ph/0510346)
Dobke B., Johnston D., Massey R., High F., Ferry M., Rhodes J., Vanderveld R., 2010, PASP, 122, 947
Eisenstein D. et al., 2001, AJ, 122, 2267
Ferry M., Rhodes J., Massey R., White M., Coe D., Mobasher B., 2008, Astroparticle Phys., 30, 65
Fukugita M., Ichikawa T., Gunn J., Doi M., Shimasaku K., Schneider D., 1996, AJ, 111, 1748
Fu L. et al., 2008, A&A, 479, 9
Gunn J. et al., 1998, AJ, 116, 3040
Hamana T. et al., 2003, ApJ, 597, 98
Hao C. N., Mao S., Deng Z. G., Xia X. Y., Wu H., 2006, MNRAS, 370, 1339
Heymans C. et al., 2006, MNRAS, 368, 1323
High F., Rhodes J., Massey R., Ellis R., 2007, PASP, 119, 1295
Hirata C., Seljak U., 2003, MNRAS, 343, 459
Hirata C. et al., 2004, MNRAS, 353, 529

Hoekstra H., 2007, MNRAS, 379, 317
Hoekstra H., Jain B., 2008, Ann. Rev. Nuclear and Particle Science, 58, 99
Hogg D., Finkbeiner D., Schlegel D., Gunn J., 2001, AJ, 122, 2129
Ilbert O. et al., 2009, ApJ, 690, 1236
Ivezić Ž. et al., 2004, Astron. Nachr., 325, 583
Kaiser N., 2000, ApJ, 537, 555
Kaiser N. et al., 2010, Proc. SPIE, 7733, 12
Kaiser N., Squires G., Broadhurst T., 1995, ApJ, 449, 460
Kasliwal M., Massey R., Ellis R., Miyazaki S., Rhodes J., 2008, ApJ, 684, 34
Kitching T. et al., 2010, preprint (arXiv:1009.0779)
Koekemoer A. et al., 2007, ApJS, 172, 196
Koekemoer A., Fruchter A., Hook R., Hack W., 2002, The 2002 HST Calibration Workshop: Hubble after the Installation of the ACS and the NICMOS Cooling System, eds. Arribas, Koekemoer, & Whitmore, p. 337
Kormendy J., Fisher D. B., Cornell M. E., Bender R., 2009, ApJS, 182, 216
Kovač K. et al., 2010, ApJ, 708, 505
Kron R., 1980, ApJS, 43, 305
LSST Science Collaborations, 2009, preprint (arXiv:0912.0201)
Lauer T. R., 1985, MNRAS, 216, 429
Leauthaud A. et al., 2007, ApJS, 172, 219
Leauthaud A. et al., 2011, preprint (arXiv:1104.0928)
Lupton R., Gunn J., Ivezić Z., Knapp G., Kent S., 2001, ASP Conf. Ser., 238, 269
Mandelbaum R. et al., 2005, MNRAS, 361, 1287
Mantz A., Allen S., Ebeling H., Rapetti D., 2008, MNRAS, 387, 1179
Marleau F., Simard L., 1998, ApJ, 507, 585
Massey R. et al., 2007a, MNRAS, 376, 13
Massey R., Rowe B., Refregier A., Bacon D. J., Bergé J., 2007b, MNRAS, 380, 229
Massey R., Kitching T., Richard J., 2010a, Rep. Prog. Phys., 73, 086901
Massey R., Stoughton C., Leauthaud A., Rhodes J., Koekemoer A., Ellis R., Shaghoulian E., 2010b, MNRAS, 401, 371
Melchior P., Böhnert A., Lombardi M., Bartelmann M., 2010, A&A, 510, A75
Miller L., Kitching T., Heymans C., Heavens A., van Waerbeke L., 2007, MNRAS, 382, 315
Miyazaki S. et al., 2002, PASJ, 54, 833
Miyazaki S. et al., 2006, Proc. SPIE, 6269, 9
Nakajima R., Mandelbaum R., Seljak U., Cohn J. D., Reyes R., Cool R., 2011, preprint (arXiv:1107.1395)
Okabe N., Takada M., Umetsu K., Futamase T., Smith G., 2010, PASJ, 62, 811
Padmanabhan N. et al., 2008, ApJ, 674, 1217
Park S., Schowengerdt R., 1983, Comp. Gr. Im. Proc., 23, 258
Pier J., Munn J., Hindsley R., Hennessy G., Kent S., Lupton R., Ivezić Ž., 2003, AJ, 125, 1559
Refregier A., 2003a, ARA&A, 41, 645
Refregier A., 2003b, MNRAS, 338, 35
Refregier A., Bacon D., 2003, MNRAS, 338, 48
Reyes R., Mandelbaum R., Seljak U., Baldauf T., Gunn J., Lombriser L., Smith R., 2010, Nature, 464, 256
Rhodes J., Refregier A., Groth E., 2000, ApJ, 536, 79
Rhodes J. et al., 2007, ApJS, 172, 203
Richards G. et al., 2002, AJ, 123, 2945
Rines K., Diaferio A., Natarajan P., 2007, ApJ, 657, 183
Rozo E. et al., 2010, ApJ, 708, 645
Sargent M. et al., 2007, ApJS, 172, 434
Schlegel D., Finkbeiner D., Davis M., 1998, ApJ, 500, 525
Schrabback T. et al., 2007, A&A, 468, 823
Schrabback T. et al., 2010, A&A, 516, A63
Schulz A., Mandelbaum R., Padmanabhan N., 2010, MNRAS, 408, 1463
Scoville N. et al., 2007a, ApJS, 172, 1
Scoville N. et al., 2007b, ApJS, 172, 38
Sérsic J., 1968, Atlas de galaxias australes, Cordoba, Argentina: Observatorio Astronomico
Sirianni M et al., 1998, Society of Photo-Optical Instrumentation Engineers (SPIE) Conference Series, Ed. D'Odorico, S., 3355, 608
Smith J. et al., 2002, AJ, 123, 2121
Stoughton C. et al., 2002, AJ, 123, 485
Strauss M. et al., 2002, AJ, 124, 1810
Tucker D. et al., 2006, Astron. Nachr., 327, 821
Vikhlinin A. et al., 2009, ApJ, 692, 1060
Voigt L. M., Bridle S. L., Amara A., Cropper M., Kitching T. D., Massey R., Rhodes J., Schrabback T., 2011, preprint (arXiv:1105.5595)
York D. et al., 2000, AJ, 120, 1579
Zhang J., Komatsu E., 2011, MNRAS, 414, 1047

APPENDIX A: SDSS IMAGING PROPERTIES USED FOR SIMULATIONS

In order to mimic SDSS data, we have determined several properties of the SDSS data at the position of each galaxy. While not all users will want to mimic specifically SDSS data, we include this information with the data release as well.

A1 SDSS observations of the COSMOS field

It is worth noting that there are several atypical aspects to the SDSS imaging in that region. First, the median seeing is slightly better than typical for the SDSS survey as a whole (by ~ 10 per cent) although in fact the range of seeing values is rather broad. Second, the sky level and therefore the photometric noise at fixed magnitude is higher than usual for SDSS. As a consequence, the object detection and star/galaxy separation are somewhat less efficient than in most of the survey area for $r \gtrsim 21$ or $i \gtrsim 20.6$ (for more details, see Nakajima et al. 2011).

A2 SDSS PSF

The SDSS PSF is determined for all galaxies in an SDSS field by the PSP (postage stamp pipeline) using a procedure described in Lupton et al. (2001). In brief, it involves modeling the temporally and spatially varying PSF using a Karhunen-Loéve (KL) transform, which uses a set of bright stars to determine basis functions and then to fit their coordinates to spatially varying (quadratic) functions. The infor-

mation about the basis functions and how their coefficients vary across a field is included in psField files.

Thus, for each galaxy in our COSMOS sample for which we have postage stamp images, we find its position in SDSS imaging. Some of these galaxies are too faint to be detected; however, given their position on the sky we can still determine precisely the CCD position at which they would have been detected in SDSS. Given this information, we obtain a postage stamp image of the galaxy i-band PSF using the publicly available READ_PSF C code[24] that reconstructs the basis functions and the variation of the coefficients across the field from the SDSS psField files.

A3 Photometricity

As stated previously, roughly 33 per cent of the SDSS imaging in the COSMOS field is classified as non-photometric according to the ubercalibration (Padmanabhan et al. 2008) procedure on the rerun 301 (DR8) reductions. There are four SDSS fields overlapping the COSMOS region: 1462 and 1907 include most of the galaxies, and 1458 and 2125 each cover a small fraction of the area. All of 1462 and 2125 in the COSMOS region are classified as photometric, but only part of 1907 and none of 1458 in that area are photometric. When determining the photometric offset between COSMOS and SDSS photometry we must be careful to exclude the regions that are non-photometric, and the data release includes information about photometricity.

A4 Photometric calibration

We start with the total galaxy magnitudes from COSMOS with an offset to convert from $F814W$ to SDSS i (Section 6.1). To determine the total number of i-band counts to assign to a galaxy of this magnitude, we first determine the relevant number of nanomaggies using

$$\mathrm{mag} = 22.5 - 2.5\ \log_{10}\left[\text{flux (nanomaggies)}\right]. \qquad \text{(A1)}$$

We then use the SDSS photometric calibration (in units of nanomaggies per count) from ubercal in the relevant SDSS run, camcol, and field for each position. This will allow us to generate images with units of counts per pixel.

A5 Noise level

When determining the level of noise to put into the fake data, we ignore the noise in the COSMOS observations, which is very small relative to that in SDSS (as stated in Sec. 5.2, the faintest magnitude that we use in COSMOS corresponds to a minimum $S/N \sim 50$, and most are > 100). Accounting for it in detail would be quite challenging given that it exhibits non-negligible pixel-to-pixel correlations after we convolve it with the SDSS PSF. We have confirmed that for these S/N levels, the noise fields that result from adding the desired level of uncorrelated Gaussian noise are statistically consistent with the noise fields we hope to introduce; that is, the KS test shows no deviations due to the noise in the original COSMOS postage stamps.

For these simulations, we approximate the noise in SDSS as being a random, uncorrelated Gaussian noise field with variance given by

$$\sigma^2_{\rm sky} = \frac{\rm sky}{\rm gain} + \sigma^2_{\rm dark}, \qquad \text{(A2)}$$

where the first term results from the Poisson noise due to the photons in the sky, and the second is due to the dark current (current that builds up due to heat even in the absence of photons).

[24] http://www.astro.princeton.edu/~rhl/readAtlasImages.tar.gz